J. Fluid Mech. (1984), *vol.* 144, *pp.* 231–280
Printed in Great Britain

Local isotropy and the decay of turbulence in a stratified fluid

By A. E. GARGETT,
Institute of Ocean Sciences, Patricia Bay, P.O. Box 6000, Sidney, B.C., V8L 4B2, Canada

T. R. OSBORN
U.S. Naval Postgraduate School, Monterey, CA 93940, U.S.A.

AND P. W. NASMYTH
Institute of Ocean Sciences, Patricia Bay

(Received 7 September 1983 and in revised form 5 March 1984)

The validity of the assumption of local isotropy is investigated using measurements of three orthogonal components of the turbulent velocity fields associated with initially high-Reynolds-number geophysical turbulence. The turbulent fields, generated by various large-scale internal motions caused by tidal flows over an estuarine sill, decay under the influence of stable mean density gradients. With measurements from sensors mounted on a submersible, we examine the evolution of spectral shapes and of ratios of cross-stream to streamwise components, as well as the degree of high-wavenumber universality, for the observational range of the parameter $I \equiv k_s/k_b = l_b/l_s$. This ratio is a measure of separation between the Kolmogoroff wavenumber $k_s \equiv (\epsilon/\nu^3)^{\frac{1}{4}} \equiv 2\pi/l_s$ typical of scales by which turbulent kinetic energy has been dissipated (at rate ϵ), and the buoyancy wavenumber $k_b \equiv (N^3/\epsilon)^{\frac{1}{2}} \equiv 2\pi/l_b$ typical of scales at which the ambient stratification parameter $N \equiv (-g\rho_z/\rho_0)^{\frac{1}{2}}$ becomes important. For values of I larger than ~ 3000, inertial subranges are observed in all spectra, and the spectral ratio ϕ_{22}/ϕ_{11} of cross-stream to streamwise spectral densities reaches the isotropic value of $\frac{4}{3}$ for about a decade in wavenumber. As k_s/k_b decreases, inertial subranges vanish, but spectra of the cross-stream and streamwise components continue to satisfy isotropic relationships at dissipation wavenumbers. We provide a criterion for when ϵ may safely be estimated from a single measured component of the dissipation tensor, and also explore questions of appropriate low-wavenumber normalization for buoyancy-modified turbulence.

1. Introduction

Much of the progress in understanding and classifying high-Reynolds-number turbulent flows has been associated with the intuitive idea of an energy cascade, which was given form by Kolmogoroff (1941, 1962; cf. Monin & Yaglom 1975, chap. 8). Briefly it is assumed that the largest eddies of a turbulent field may be highly anisotropic as a result of the specific flow field in which they originate: however, as nonlinear processes of successive instabilities rapidly transfer energy to eddies of ever smaller scale, the 'memory' of large-scale anisotropy is lost. 'Local isotropy', as introduced by Kolmogoroff (1941), assumes that fluctuations with lengthscales much smaller than the energy-containing eddy scale are homogeneous, isotropic and (nearly) statistically stationary.

The mathematical quantity usually considered to embody the concept of energy associated with a particular scale of motion is the three-dimensional kinetic-energy spectral density (per unit mass) $E(k)$, where

$$\int_0^\infty E(k)\,\mathrm{d}k \equiv \tfrac{1}{2}(\overline{u_1^2}+\overline{u_2^2}+\overline{u_3^2}), \tag{1}$$

with the convention that u_3 is the vertical component, u_1 and u_2 the horizontal components, and u_1 is in the direction of streamwise radian wavenumber k. However, actual measurements are of one-dimensional spectral functions $\phi_{ii}(k)$ (no summation over repeated indices) defined by

$$\int_0^\infty \phi_{ii}(k)\,\mathrm{d}k = \overline{u_i^2}. \tag{2}$$

For isotropic turbulence $\overline{u_1^2} = \overline{u_2^2} = \overline{u_3^2}$, $\phi_{22}(k) = \phi_{33}(k)$, and the one-dimensional spectra are related to $E(k)$ by

$$E(k) = -k\frac{\mathrm{d}}{\mathrm{d}k}\{\tfrac{1}{2}\phi_{11}(k)+\phi_{22}(k)\} \tag{3}$$

and to each other by

$$\phi_{jj}(k) = \frac{1}{2}\left\{\phi_{11}(k) - k\frac{\partial\phi_{11}(k)}{\partial k}\right\} \quad (j = 2, 3). \tag{4}$$

The rate of kinetic energy dissipation ϵ can be expressed as various integrals over the one-dimensional dissipation functions $k^2\phi_{jj}(k)$:

$$\epsilon = 2\nu\int_0^\infty E(k)\,\mathrm{d}k = 15\nu\int_0^\infty k^2\phi_{11}(k)\,\mathrm{d}k = \tfrac{15}{2}\nu\int_0^\infty k^2\phi_{jj}(k)\,\mathrm{d}k \quad (j = 2, 3). \tag{5}$$

The idea of local isotropy asserts that the above relationships are expected to hold in high-Reynolds-number turbulence at wavenumbers sufficiently large that the turbulence has become independent of the low wavenumbers (large scales) where most of the turbulent energy resides. Kolmogoroff's first hypothesis added to local isotropy the assumption that the form of $E(k)$ in this range depends only upon k, ν and the rate at which energy is passing through the spectrum; for stationary turbulence this must equal the rate ϵ at which energy is being dissipated at the smallest scales. Dimensional arguments then require

$$E(k) = \epsilon^{\frac{2}{3}}k^{-\frac{5}{3}}F(k/k_\mathrm{s}), \tag{6}$$

where

$$k_\mathrm{s} \equiv (\epsilon/\nu^3)^{\frac{1}{4}} \tag{7}$$

and $F(k/k_\mathrm{s})$ is a universal function. This result, often called 'local similarity', can be further simplified (Kolmogoroff's second hypothesis) if the Reynold's number Re is sufficiently large that there exists a range of wavenumbers, between energy-containing and dissipation ranges, in which molecular viscosity ν is unimportant. In this inertial subrange the form of

$$E(k) = A\epsilon^{\frac{2}{3}}k^{-\frac{5}{3}} \tag{8}$$

is determined within a constant A, the three-dimensional Kolmogoroff constant. Expressions for the measured spectral functions obtained from (8) using (3) and (4) are

$$\left.\begin{aligned}\phi_{11}(k) &= A_1\epsilon^{\frac{2}{3}}k^{-\frac{5}{3}},\\ \phi_{jj}(k) &= A_2\epsilon^{\frac{2}{3}}k^{-\frac{5}{3}} \quad (j = 2, 3),\end{aligned}\right\} \tag{9}$$

where $A_1 = \frac{18}{55}A$ and $A_2 = \frac{4}{3}A_1$. The latter relationship implies that the ratio for cross-stream to streamwise spectral density is

$$\frac{\phi_{jj}(k)}{\phi_{11}(k)} = \tfrac{4}{3} \quad (j = 2, 3) \tag{10}$$

over an inertial subrange.

In a later paper, Kolmogoroff (1962) refined his original theory, allowing for spatial intermittency in the dissipation rate ϵ by a third hypothesis: that ϵ is a lognormal random variable with variance $\sigma^2 = A_0 + \mu \ln(L/r)$, where A_0 is a constant, dependent upon the particular flow geometry, μ is a universal constant, L is an integral (energy-containing) scale and r is a length characteristic of averaging volume. Yaglom (1966) subsequently derived the appropriate modification to the inertial subrange, of the form

$$E(k) = B\epsilon^{\frac{2}{3}}k^{-\frac{5}{3}}(Lk)^{-\frac{1}{9}\mu},$$

where B is a constant. Since the universal constant μ appears to be ~ 0.5 (Gibson & Masiello 1972), the predicted modification to the $-\frac{5}{3}$ exponent of the energy spectrum in the inertial subrange is virtually unobservable. Using a simple ϵ-distribution and underlying power-law subranges, Grant, Stewart & Moilliet (1962) demonstrated that the distribution of ϵ has little effect over the entire spectrum. Thus, given the accuracy of field measurements, we are unlikely to detect consequences of Kolmogoroff's third hypothesis in velocity spectral functions (although of course the same cannot be said about higher-order moments).

Evidence supporting various consequences of Kolmogoroff's theory for high-Re flows has accumulated over the past twenty years. Numerous examples of $-\frac{5}{3}$ subranges have been observed (for recent reviews see Champagne 1978; Mestayer 1982), although it has long been realized that existence of a $-\frac{5}{3}$ subrange, even with the 'correct' value of the Kolmogoroff constant, does not guarantee local isotropy (Stewart 1969; Champagne, Harris & Corrsin 1970; Busch 1973). The more stringent requirement of (4) appears more difficult to observe. Champagne (1978) reports direct confirmation of (4) only at dissipation scales for laboratory flows covering a range of 138–626 in turbulent Reynolds number $R_\lambda \equiv u\lambda/\nu$, where u is a typical r.m.s. turbulent velocity and $\lambda \equiv u^2/(\partial u/\partial x)^2$ is the Taylor microscale. Mestayer (1982) finds the same result for a laboratory flow of $R_\lambda = 616$. Gibson (1963) measured all three velocity components in a laboratory jet of somewhat higher R_λ (710–780), finding about two decades of $-\frac{5}{3}$ range in the streamwise spectrum, rather less in the cross-stream spectrum, and the predicted $\frac{4}{3}$ ratio in the range where both exhibited $-\frac{5}{3}$ ranges. Much higher values of R_λ characterize homogeneous flows in the oceans and the atmosphere. Here there appears to be a wealth of observational material, almost all of which supports local similarity, as expressed by (6). However, few field experiments have measured both streamwise *and* cross-stream velocity components through dissipation scales. Thus a direct confirmation of the underlying assumption of local isotropy (via (4) or, in an inertial subrange, the related $\frac{4}{3}$ ratio of (10)) has seldom been achieved for high-R_λ flows. Mestayer (1982) has recently cast doubt on reports of the $\frac{4}{3}$ ratio deriving from sonic anemometer measurements, leaving only the hot-wire measurements of Busch (1973) and the miniature cup-anemometer measurements of Garratt (1972), taken in the atmospheric boundary layer over land and water respectively. The wavenumber extent of the $\frac{4}{3}$ region in each case was nearly two decades (Busch) and slightly less than a decade (Garratt). Most of the observations surveyed above were taken in homogeneous flows, rather than the stratified flows

typical of the interior of both atmospheres and oceans. In such systems stable stratification, as described by the buoyancy frequency $N \equiv (-g\rho_0^{-1}\,\partial\rho/\partial z)^{\frac{1}{2}}$, enters not only as an additional field variable but as a quantity of dynamical significance. Mean stratification allows the existence of a full suite of inertio–gravity waves, so altering the pathways of energy transfer among scales that we may no longer expect simplistic energy cascades. Moreover, for given available kinetic energy (per unit mass) $E = \frac{1}{2}U^2$, simple energy arguments suggest that mean stratification decreases the vertical overturning scale, hence the Reynolds number, from that typical of an unstratified fluid. It might be imagined that the idea of local isotropy has little place in such systems, but the measurements of Busch (1973), some of which were taken in stably stratified conditions, suggest otherwise. Moreover, Tennekes (1973) shows that a gradient Richardson number characteristic of dissipation scales is very small, so that the small-scale structure of turbulence should be independent of hydrostatic stability. Although his argument is somewhat weakened if the fluid Prandtl number $Pr \equiv \nu/\kappa$ is larger than unity, it seems reasonable that it is the smaller scales of turbulence (if any) that may achieve local isotropy despite the macroscopic properties of the mean flow, including its mean stability N. Thus the concept of local isotropy may prove useful (in the sense of furnishing quantitative predictive ability) even in stratified flow.

A main purpose of this paper is to investigate the concept of local isotropy for turbulence in a strongly stratified fluid. Since it is clear that stratification must eventually inhibit large (vertical) scales, it is also of interest to discover an appropriate scaling for energy-containing eddies of a buoyancy-modified turbulent field. A simple scaling arises if one assumes that only two parameters are important to a description of these energy-containing scales; namely N, representing the strength of the stratification, and ϵ, representing the strength of nonlinear interactions by which energy is transferred to dissipation scales. By dimensional analysis, one then obtains a buoyancy-wavenumber scale

$$k_b \equiv \left(\frac{N^3}{\epsilon}\right)^{\frac{1}{2}} \tag{11}$$

(with associated lengthscale $l_b = 2\pi/k_b$), and a buoyancy-velocity scale

$$u_b \equiv \left(\frac{\epsilon}{N}\right)^{\frac{1}{2}}. \tag{12}$$

A physical meaning for the scale k_b was apparently first discussed by Dougherty (1961) (who credits the idea to R. W. Stewart: similar discussions may be found in Ozmidov (1965) and Gibson (1980)). Since the provenance of k_b is unclear, we have chosen to call it simply the buoyancy wavenumber. Dougherty assumed that at sufficiently high wavenumbers the Kolmogoroff theory of inertial turbulence holds, so that the energy spectrum has the form $E(k) \propto \epsilon^{\frac{2}{3}}k^{-\frac{5}{3}}$ (equation (8)). The kinetic energy per unit mass due to motions of scale $L \propto k^{-1}$, obtained by integrating $E(k)$ over a unit bandwidth centred at k, is then K.E. $\propto \epsilon^{\frac{2}{3}}k^{-\frac{2}{3}}$. The potential energy per unit mass associated with such a scale is P.E. $\propto N^2L^2 \propto N^2k^{-2}$, so that a scale-dependent Richardson number becomes

$$Ri(k) \propto N^2\epsilon^{-\frac{2}{3}}k^{-\frac{4}{3}} = \left(\frac{k}{k_b}\right)^{-\frac{4}{3}}.$$

For $k \gg k_b$, $Ri(k) \to 0$, and hence buoyancy forces are negligible (as initially assumed in the form for $E(k)$). As $k \to k_b$, $Ri(k)$ increases, and eventually exceeds the necessary condition for stability (Miles & Howard 1964). Thus $k \sim k_b$ is an appropriate scaling for the largest eddies that are able to overturn, given the background stratification.

The associated velocity scale is derived by assuming that a length proportional to l_b is an appropriate 'outer' lengthscale L to use in the scale relationship

$$\epsilon \propto \frac{u^3}{L}$$

known to apply to homogeneous turbulence (Tennekes & Lumley 1972). The result is that $u \sim (\epsilon l_b)^{\frac{1}{3}} = (\epsilon/N)^{\frac{1}{2}} \equiv u_b$ is the appropriate scaling velocity for the largest eddies.

Buoyancy velocity and lengthscales may be combined to form a buoyancy-modified Reynolds number (Dillon & Caldwell 1980)

$$R_b \propto \frac{u_b l_b}{\nu} = \frac{\epsilon}{\nu N^2},$$

where we use a proportional sign, rather than an equality, to indicate that appropriate velocity and lengthscales may differ from u_b and l_b by $O(1)$ constants. R_b could be used to classify turbulent flows in a stably stratified fluid, just as R_λ is used to classify homogeneous flows. However we preferred to use the parameter

$$I \equiv \frac{k_s}{k_b} = \frac{l_b}{l_s} \propto R_b^{\frac{3}{4}}, \tag{13}$$

which is the ratio of Kolmogoroff wavenumber to buoyancy wavenumber (or buoyancy wavelength $l_b \equiv 2\pi/k_b$ to Kolmogoroff wavelength $l_s \equiv 2\pi/k_s$). Since l_s is a characteristic dissipation scale,† and we expect that l_b is proportional to a characteristic (vertical) energy-containing scale, I has the straightforward interpretation of separation between scales (wavenumbers) at which energy is fed into turbulence and those at which energy is dissipated. Since sufficient separation of these scales is a condition for existence of inertial subrange, I seems (and proves) to be a reasonable basis for classification of turbulence in a stratified environment.

This paper will first examine indications of the degree of isotropy achieved in geophysical turbulence generated by various instabilities of oceanic internal waves, stratified flows quite different from the steady uniform boundary layers of meteorological observations. Section 2 briefly describes the two flow regimes in which measurements were made, while §3 describes various characteristics of the velocity instrumentation and the submersible vehicle on which it was mounted, as well as the technique used to estimate N from submersible-based sensors (readers disinterested in instrumentation may wish to skip §3.1). In §§4 and 5 we examine records with a wide range of I-values for evidence of local isotropy, local similarity and inertial subranges. The Class 1 records ($I \gtrsim 3000$) of §4 exhibit various characteristics of high Reynolds-number turbulence: clear $-\frac{5}{3}$ ranges in all three component spectra and a value of $\frac{4}{3}$ for both ratios of cross-stream/stream-wise spectra for over a decade before dissipation scales. In addition, spectra satisfy (4) over the entire range of measurement. In §5 we follow the evolution of the Class 1 spectral shapes and ratios as I decreases. The maintenance of dissipation-scale isotropy over the observed range of I-values has implications for direct measurement of ϵ in the stratified ocean and atmosphere.

† We note that many authors choose to define lengthscales $L_s = 1/k_s$ and $L_b = 1/k_b$ which are *smaller* than l_s and l_b by a factor of 2π, hence have associated radian wavenumbers $K_s = 2\pi/L_s$ and $K_b = 2\pi/L_b$ which are 2π times *larger* than k_s and k_b. Since this can cause considerable confusion, we would like to clarify that our reason for choosing k_s is the observation that velocity-gradient (dissipation) spectra approach zero by $k = k_s$ (not $2\pi k_s$); hence l_s is clearly a more appropriate dissipation lengthscale than L_s. Our use of k_b is consistent with k_s.

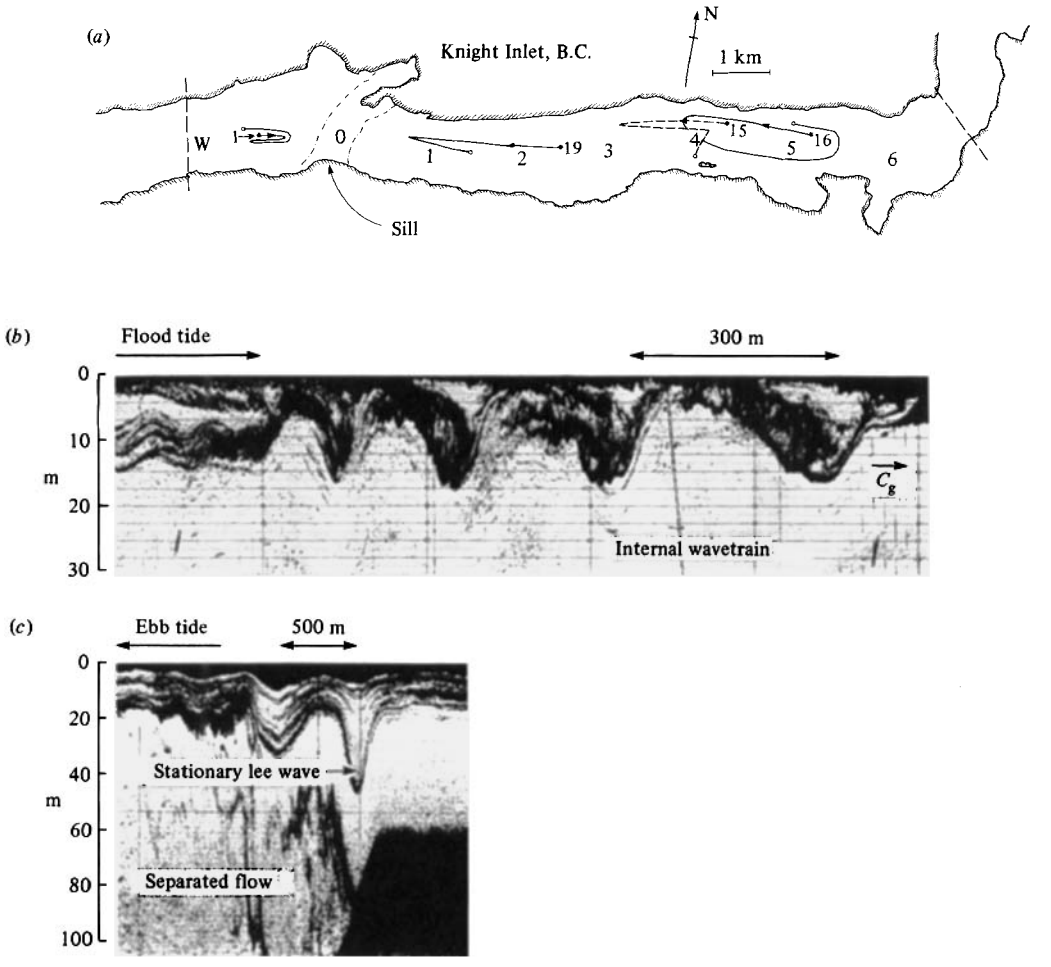

FIGURE 1. (*a*) Plan section of a portion of Knight Inlet, showing the location of the sill which divides the inlet into two basins. Turbulence measurements were taken from a submersible vehicle operating in the region between the dashed lines during the week of 15–22 November 1978. Submersible tracks shown (identified by date) supplied data used in this paper. Marked stations (W and 0–5) are locations of CTD profiles. (*b*, *c*) The two flow regimes in which measurements were taken are shown here (courtesy of David Farmer) in records from a 200 kHz echo-sounder operated during the week of turbulence measurements (horizontal scales are approximate): (*b*) measurements to the east of the sill were taken in an internal wave train released from the sill on the turn to flood tide; (*c*) To the west of the sill, measurements were taken in separated flow downstream of the sill on ebb tide.

Section 6 examines the low-wavenumber buoyancy scaling mentioned above, while §7 attempts to relate the present measurements to various laboratory experiments in stratified turbulence.

2. Flow regimes in Knight Inlet

Knight Inlet, a fjord on the western coast of Canada, is separated into two basins by a sill rising to 60 m depth across the entire width of the inlet (figure 1*a*). Mixing processes appear to be dominated by a variety of internal hydraulic phenomena

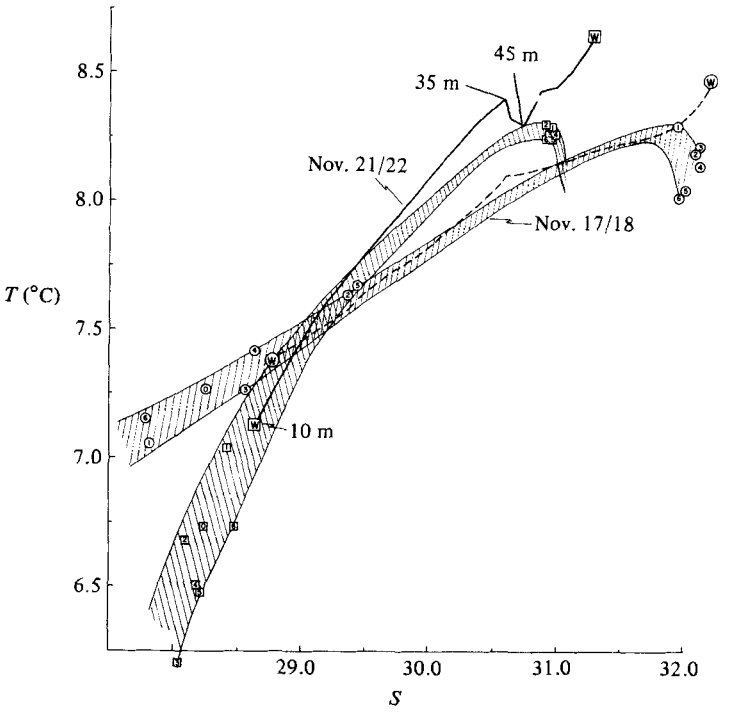

FIGURE 2. Evolution of (T, S)-characteristics in the observational area over a four day period. The single profile available on the western (W) side of the sill is plotted as a line, while the group of six stations over the sill (0) and progressively further east (1–5) lie within the envelopes at each time period. Values at 5 m and 100 m depths are noted for each station in circles (17, 18 November) or boxes (22 November) near the lower-left and upper-right ends of the envelopes (with the exception of station W, for which 5 m values are not available). Seasonal cooling has reduced the temperature of near-surface water, while internal mixing processes like those shown in figure 1 have slightly increased the temperature and dramatically reduced the salinity of the deeper water.

associated with tidal flows over this sill (Farmer & Smith 1980; Freeland & Farmer 1980).

Turbulence measurements were taken through the two types of flow depicted in the acoustic images of figures 1 (*b*, *c*). With the tidal amplitudes and stratification of the measurement period, ebb flow over the sill produces flow separation behind the sill and a mode 1 lee wave just above the separation point. As the ebb flow slackens, this original lee wave moves upstream over the sill crest and subsequent waves form behind it. On flood tide, the resulting wavetrain leaves the sill and propagates up-inlet at a speed of ~ 0.5 m/s (Farmer & Smith 1977). The acoustic images reveal a wealth of small-scale 'turbulent' structures in the separated ebb flow and, increasing with distance from the sill, within the propagating internal wavetrain. The measurements reported here prove conclusively that these structures are indeed evidence of turbulence.

One consequence of these vigorous mixing processes is that (T, S)-properties in the upper waters of the inlet change rapidly with time. Figure 2 illustrates this with two groups of (T, S)-curves from stations marked in figure 1 (*a*). Stations in each group were taken within a time period of 4 h or less, and the groups are 4 days apart (Anon. 1979). Over 4 days, near-surface ($z < 20$ m) waters have become significantly colder, while the deeper ($z > 100$ m) waters have become slightly warmer and markedly

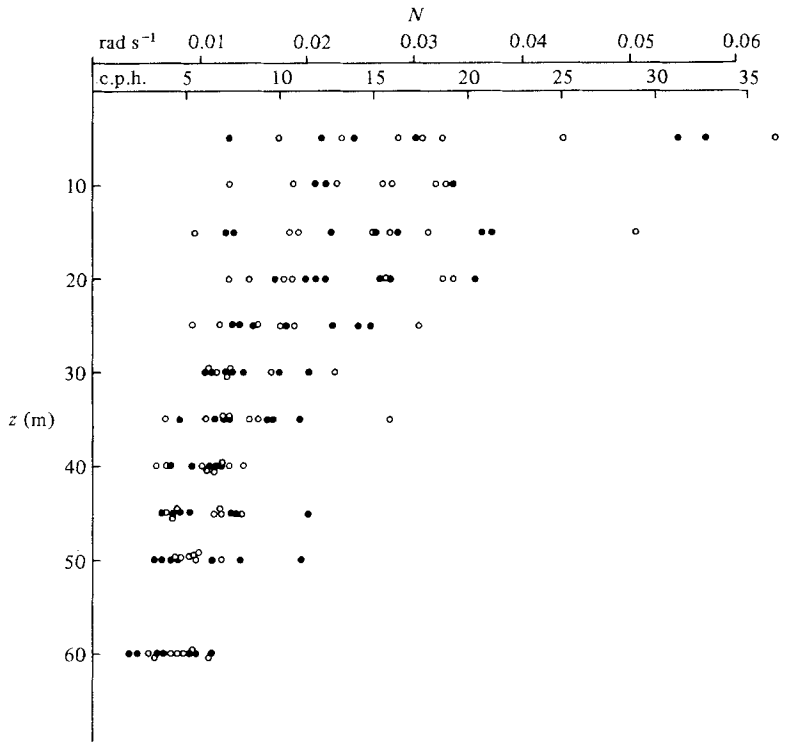

FIGURE 3. Buoyancy frequency N estimated from CTD measurements in the observational area of Knight Inlet. The stations are those used for the (T, S)-plots of figure 2, taken on 17, 18 November (open circles) and 22 November (dark circles). There has been no observationally significant change in N. despite the significant changes in (T, S)-structure noted in figure 2.

fresher. This is true for stations both west (W) and east of the sill, even though these exhibit and maintain clear differences in deep water (T, S)-characteristics: deeper water in the inner basin is colder and fresher than that in the outer basin.

Despite these changes in (T, S)-characteristics, the mean stability of the water column is not noticeably affected: within the scatter of N estimates plotted as a function of depth in figure 3 there is no obvious division between the two groups of stations. Values are generally 10–20 c.p.h. between 5 and 20 m depth, decreasing to a range of $\sim$ 4–7 c.p.h. by 50 m depth. Very large values ($N > 30$ c.p.h.) are typically found at depths less than 5 m at those stations furthest up-inlet, due to increased fresh-water component from run-off entering primarily at the head of the inlet. In CTD stations taken at random relative to internal wave phenomena, such large N-values may occasionally be encountered at greater than average depths; this effect almost certainly accounts for the few very large values observed at 5 m depth.

3. Instrumentation

The Knight Inlet turbulence measurements were made with a set of sensors (shown schematically in figure 4), carried $\sim$ 3 m in front of the research submersible *Pisces IV*. Four high-frequency sensors mounted at the forward tip of the instrument package measured streamwise velocity component u with a heated conical platinum film probe, orthogonal cross-stream velocity components v, w with airfoil probes,

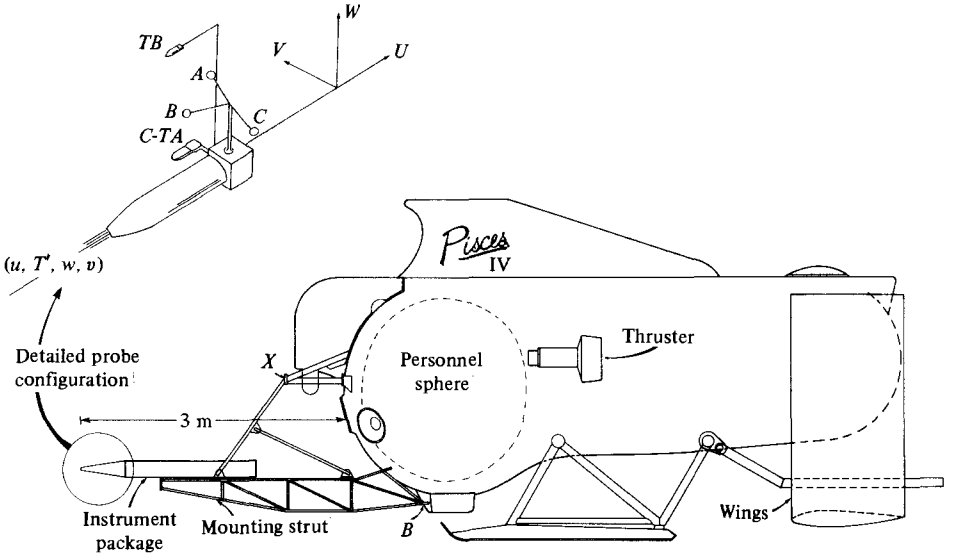

FIGURE 4. Schematic diagram of the submersible *Pisces IV* used to carry turbulence sensors. The inset shows the configuration of probes in a submersible-based coordinate system.

and temperature T' with a cold conical platinum-film probe. Essential supporting information were low-frequency velocity components U, V, W from a triplet of ducted rotors A, B, C located slightly behind (0.33 m) and above (0.5 m) the leading sensors, water temperature T_A and conductivity C measured at the same level as the high-frequency temperature sensor, and temperature T_B measured 0.8 m directly above T_A. A pressure sensor within the submersible and three accelerometers mounted in an orthogonal jig attached to the front end of the instrument package, 0.3 m behind the high-frequency probes, completed the instrumentation. The present description of sensor characteristics and performance will be sufficient to assess accuracy of measurements of velocity buoyancy frequency: further details of instrumentation may be found in Gargett (1980), and a general discussion of the submersible vehicle is given by Gargett (1982). In the following discussions, notation is the same as that used in figures 5(*a*, *b*), typical records from the suite of sensors operating in the separated flow west of the sill and in the internal wavetrain respectively.

3.1. *Velocity measurements*

Heated-film probe

The specific heated-film sensor (V30) used in these measurements is one of those manufactured at the University of British Columbia for use by the Pacific Naval Laboratory (Grant *et al.* 1962). The sensing element is a thin ring of platinum deposited around a conical glass probe and protected by a very thin quartz coating. Speed fluctuations parallel to the probe axis produce fluctuations in heat transfer from the film which are sensed by an a.c. bridge operated in constant-temperature mode (appropriate for the oceanic application, where plankton or detrital material may lodge on the probe, greatly reducing heat transfer: under these circumstances, a constant-current bridge would burn out the probe). The bridge is an a.c. feedback loop which maintains the probe at a constant number of degrees (the overheat Δ) above ambient temperature. The temperature coefficient of resistance, measured for

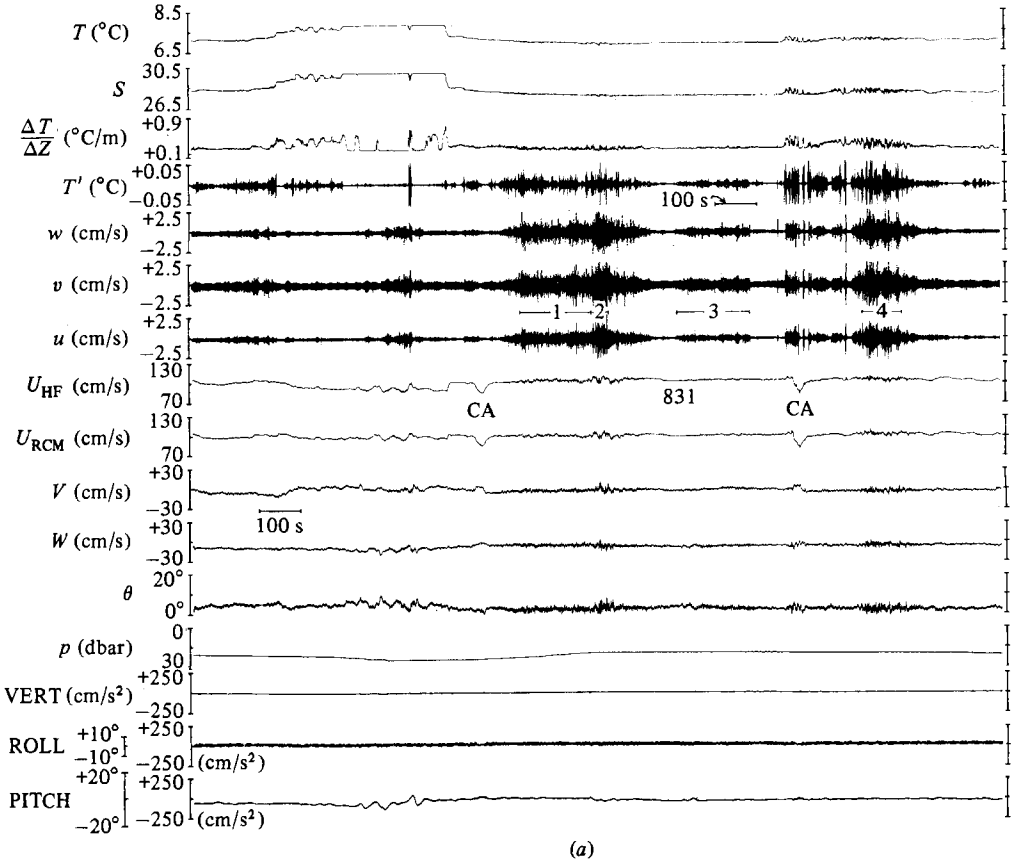

(*a*)

FIGURE 5. (*a*) Signals recorded as *Pisces IV* travelled within separated boundary flow west of the sill (W in figure 1). Signals are plotted as functions of time from left to right: because of *Pisces*' near-constant mean forward speed of ~ 1 m s^{-1}, they may as well be considered functions of distance, with 100 s $\approx$ 100 m. T and S are temperature and salinity measured at the level of the high-frequency sensors. $\Delta T/\Delta Z$ is an estimate of local vertical temperature gradient obtained by differencing the output of thermistors T_A and T_B (figure 4). T' is output from the cold-film temperature probe between 1 and 100 Hz, the same passband used for the vertical (w) and horizontal (v) cross-stream velocities measured by airfoil probes, and the horizontal streamwise velocity component (u) measured by the heated film. U_{HF} is a separate recorded version of the heated-film signal which contains velocity information to zero frequency. Immediately below it is U_{RCM}, an independent measure of forward speed calculated from a triplet of small ducted rotors located slightly behind and above the heated-film. V and W are horizontal and vertical cross-stream components of the flow as measured by these rotors, while θ is the instantaneous total angle of attack between the mean flow and the high-frequency sensors: an average value of $\theta \lesssim 10°$ is sufficient for proper performance of both heated-film and airfoil sensors. Pressure p and three components of acceleration are measured by sensors at the same level but slightly behind the high-frequency sensors. The thickness of the accelerometer trace is due to submersible-produced vibrations.

This record and that of (*b*) display the various features of submersible and instrument performance referred to throughout §3. CA denotes short periods when the horizontal course of the submersible was adjusted by running only one thruster (hence the drop in forward speed).

Sample lengths marked by a numeral are among those identified within the text by Tape-File-Starting block-M, where $M/0.24414$ is the record length in metres. Records marked in (*a*) are:

Record 1 = 831-1-3925-41 (168 m); Record 2 = 831-1-4760-9 (37 m);
Record 3 = 831-2-150-42 (172 m); Record 4 = 831-2-2355-23 (94 m).

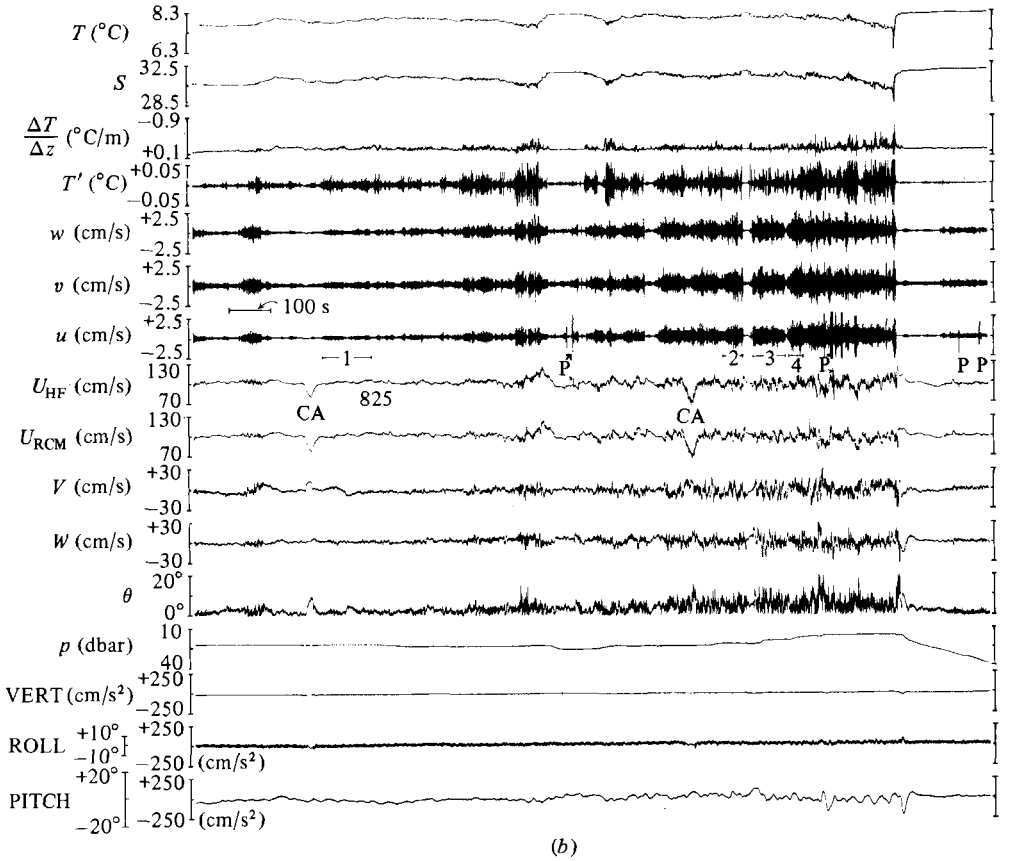

(*b*)

(*b*) Signals recorded as *Pisces IV* travelled through an internal wavetrain from the rear (left), passing through the leading edge at the position near the right of this figure where T and S rise sharply and the high-frequency signals abruptly drop to near noise-level. The subsequent steep descent of the pressure trace occurs as the submersible is caught in strong downward motion in front of the internal wave train. The signals are described above in (*a*). P indicates the effect on heated-film output of probe encounters with 'plankton' (see §3.1).

Records marked in (*b*) are:

Record 1 = 825-1-3400-29 (119 m); Record 2 = 825-2-2350-12 (49 m);
Record 3 = 825-2-2725-18 (74 m); Record 4 = 825-2-3150-10 (41 m).

each probe individually, is used to calculate R_A, the resistance change that corresponds to a given overheat. In operation, the bridge is first balanced (resistance and capacitance) with the probe moving through the water, then R_A is added to the 'cold' resistance of the probe, and this 'hot' resistance is set on the bridge resistance arm. The servo-loop is then opened, and a final adjustment made to the reactive balance. Thereafter the probe operates at constant overheat provided that the ambient water temperature doesn't change: the error associated with this assumption is discussed below. Output from the hot-film bridge varies with total flow past the sensor, and thus contains mean-flow as well as higher-frequency information. Considerations of dynamic range result in splitting the signal into two parts. One channel (U_{HF}) is low-pass filtered (3 db at 0.5 Hz), while a second channel (u) has mean bridge voltage at the operating speed (~ 1 m s^{-1}) removed and high frequencies boosted by a

prewhitening filter before digitization. The high-frequency channel is sampled at 1000 Hz, resulting in a nominal frequency (wavenumber) pass band of 0–500 Hz (0–500 c.p.m. at 1 m s^{-1}) for the measurement of streamwise velocity. Physical size of the sensitive film (diameter ~ 0.07 cm) is not a limiting factor within this range.

The response function of the hot-film probe/bridge system is completely determined by laboratory calibrations carried out in a low-turbulence-level recirculating water tunnel both before and after each cruise.

(*a*) Output of the system is determined as a function of *steady* mean flow: the resulting calibration curve is fitted by a fourth-order polynomial which can be differentiated to provide $S_0(f = 0, U)$ in V/(cm s^{-1}), the zero-frequency sensitivity as a function of mean speed.

(*b*) Response of the probe as a function of frequency $S_D(f, U)$ is determined experimentally using the vibrator technique (Grant *et al.* 1962), in which the probe is vibrated sinusoidally parallel to its axis at different frequencies within the range of interest. The r.m.s. bridge output voltage divided by $2\pi fd$, the r.m.s. velocity experienced by a probe vibrating sinusoidally at frequency f through r.m.s. displacement d (measured by a displacement transducer), yields $S_D(f, U)$. The vibrator cannot produce accurately sinusoidal displacements at frequencies much less than 20 Hz: above this frequency, measured $S_D(f, U)$ for V30 is approximately flat to ~ 50 Hz, then rises for higher frequencies as a result of the particular probe geometry (Lueck 1979). The *shape* of $S_D(f, U)$, obtained by normalizing to unity at any frequency within the flat part of the response curve ($20 < f < 50$ Hz), is invariant within measurement accuracy (1–5%) over a range of mean flow values of 0.8–1.0 m s^{-1}. Over this range of U, actual values of S_D determined at 30 and 50 Hz are typically $\sim 7\%$ higher than $S_0(f = 0, U)$, implying that the response rises (we assume linearly) by $\sim 7\%$ between zero frequency and 20 Hz, the lowest frequency of direct response measurement.

In many flow situations, the heated-film is a highly nonlinear speed sensor. An advantage of the present application is that vehicle forward speed is generally constant to within ± 5–10 cm s^{-1}, while fluctuating levels at frequencies above 1 Hz seldom exceed ± 1 cm s^{-1}. These circumstances allow assumption of local linearity (constant gain) without introducing an error larger than those involved in the experimental determination of sensitivity. Thus with *Pisces* travelling at mean speed U, one may convert raw power-spectral density (V^2/c.p.s.) of the high-frequency channel to physical units ((cm $s^{-1})^2$/c.p.s.) by dividing by $(S_0(f = 0, U)\, P(f)\, W(f))^2$, where $P(f)$ is the (re)normalized (to 1.0 at $f = 0$) response as a function of frequency and $W(f)$ is the response of the prewhitening filter.

Heated-film probes are notoriously difficult to operate successfully in the marine environment: common problems are (i) probe instability, (ii) fouling by plankton or detrital material, and (iii) temperature contamination. These problems either do not exist or are minimized by various factors in the present set of measurements.

(i) The stability of V30 was checked by running complete calibrations both before and after field operations (in which the probe was operated for approximately 20 h). Within the errors ($\sim \pm 5\%$) of the calibration techniques, the two sets of calibrations are indistinguishable (Gargett 1980).

(ii) Data loss due to fouling was minimized by working in November, a period of relatively low biological productivity, and in the upper 0–30 m of the water column during daylight hours. Remaining problems with material of presumably biological origin, which we rather broadly term 'plankton', were infrequent and easy to identify on one or other of the heated-film channels. The low-pass channel U_{HF} afforded a

very sensitive indication of fouling when compared with U_{RCM} measured by the rotor triplet. These two estimates usually agreed within a few percent. In the few cases where differences greater than 10 % were observed, it was generally possible to look back in the record of U_{HF} and identify an abrupt change in level due to biological material sticking to the probe. Such a coating affects the heat-transfer properties of the boundary layer over the film, and subsequent velocity measurements, although not obviously different in character, are certainly not well calibrated until it is removed: we do not use such data. In the work of Grant *et al.* (1968) and Nasmyth (1970), 'plankton' removal was accomplished by washing the probe with a high-speed water jet whenever a level change was noticed in U_{HF}. In *Pisces*, limited display capability made it impossible to monitor U_{HF}. Fortunately, however, probe washing happened automatically in crossflows generated when the submersible's horizontal course was altered. Since this happened frequently (*CA* in figure 5), the probe was never fouled for extended periods of time.

Another 'plankton' effect is a large 'spike' which occurs when material simply passes through the heated boundary layer without sticking (*P* in figure 5*b*). Such features are best identified on the high-frequency channel, and are avoided when selecting data for analysis. Plankton spiking was not a serious problem in the upper waters of Knight Inlet, but increased dramatically below $\sim$ 90 m.

(iii) To first order, temperature contamination is minimized by the fact that the total temperature range in the upper 100 m of Knight Inlet is only ~ 2 °C: furthermore, since the velocity bridge was initially balanced at the mean depth and temperature of planned measurements, *changes* in mean temperature are closer to ~ 1 °C (see figure 5). Since the measured zero-frequency temperature sensitivity of the probe is $(\mathrm{d}U/\mathrm{d}T)_{f=0} \approx 15$ cm s^{-1}/°C, such changes of water temperature could account for differences that are occasionally observed between mean values of U_{HF} and U_{RCM}.

It is, however, the temperature sensitivity at higher frequencies that is of concern to the present measurements. That is undoubtedly smaller than $(\mathrm{d}U/\mathrm{d}T)_{f=0}$ because, while velocity fluctuations directly modify the boundary layer over the film, temperature fluctuations must diffuse through it. For a change of 1 °C, we measured a change in the sensitivity $S_0(f = 0, U = 1 \text{ m s}^{-1})$, i.e. the *slope* of the steady calibration curve at the mean speed of *Pisces* measurements, of only 3.5 % compared with the 15 % change in mean speed. Thus we use a value of $(\mathrm{d}U/\mathrm{d}T) \simeq 3.5$ cm s^{-1}/°C as an estimate of temperature sensitivity in the frequency range of interest to the present measurements. An estimate of the possible percentage error in the axial velocity component spectrum ϕ_{11} due to temperature contamination is

$$E_T = \left(\left(\text{r.m.s. } T\left(\frac{\mathrm{d}U}{\mathrm{d}T}\right)\right)\Big/\text{r.m.s. } u\right)^2 \times 100\,\%.$$

Using r.m.s. u and r.m.s. T calculated from the hot-film and cold-film signals at frequencies greater than 0.5 Hz, this estimate rarely exceeds 1 % (table 1), leading us to conclude that temperature contamination is unlikely to be of importance to the ϕ_{11} spectrum.

A final aspect of the probe is its response as a function of total angle of attack θ between probe axis and mean-current vector $\boldsymbol{U}$. A special angular jig allowed direct measurement of the probe response for $|\theta| \leqslant 20°$; within ± 3 cm s^{-1} of a mean speed of 1 m s^{-1}, probe response is flat over this angular range. This is a useful property if the aim is to measure fluctuations due to isotropic turbulence from a platform which might develop sizeable angles between probe axis and $\boldsymbol{U}$, conditions typical of towed

		(i)			(ii)			
Class	Record	r.m.s. (u) cm s^{-1}	r.m.s. (T) (°C)	E_T (%)	a	s	$\frac{\phi_{11}}{\phi_{33}}$	E_w (%)
1	822-1-1030-19	3.0	3.2×10^{-2}	1.1×10^{-1}	−1.05°	−0.71°	1.17	1.1×10^{-1}
	825-2-2350-12	2.6	1.7×10^{-2}	5.2×10^{-2}	−0.16°	−1.22°	1.30	1.4×10^{-2}
	825-2-2725-18	2.7	1.9×10^{-2}	6.1×10^{-2}	−0.92°	+1.57°	1.06	2.0×10^{-1}
	825-2-3150-10	3.1	2.5×10^{-2}	8.0×10^{-2}	−0.06°	+2.47°	0.69	1.2×10^{-1}
2	832-1-4000-20	8.9×10^{-1}	3.7×10^{-3}	2.1×10^{-2}	−4.05°	−0.65°	1.55	1.0
	826-3-4500-42	1.4	6.3×10^{-3}	2.5×10^{-2}	−1.34°	−0.54°	1.41	1.5×10^{-1}
	839-1-3050-29	1.4	2.2×10^{-2}	3.0×10^{-1}	1.06°	0.86°	2.00	2.2×10^{-1}
	831-1-4760- 9	1.5	2.0×10^{-2}	2.2×10^{-1}	−3.30°	−1.12°	1.60	9.5×10^{-1}
3	831-2-2355-23	1.2	2.7×10^{-2}	6.2×10^{-1}	−2.21°	−0.53°	1.92	4.4×10^{-1}
	831-1-3925-41	9.6×10^{-1}	1.2×10^{-2}	1.9×10^{-1}	−2.55°	0.92°	2.95	2.4×10^{-1}
	832-1-4975-24	5.9×10^{-1}	2.4×10^{-3}	2.0×10^{-2}	−375°	−0.21°	1.90	9.1×10^{-1}
	837-2-4100-15	7.9×10^{-1}	1.4×10^{-2}	3.8×10^{-1}	3.43°	−0.40°	3.28	9.2×10^{-1}
4	838-1- 220-23	5.1×10^{-1}	6.6×10^{-3}	2.1×10^{-1}	2.85°	1.26°	2.98	1.5
	825-1-3400-29	5.7×10^{-1}	8.9×10^{-3}	3.0×10^{-1}	1.22°	−0.45°	3.48	6.3×10^{-2}
	831-2- 150-42	5.1×10^{-1}	6.8×10^{-3}	2.2×10^{-1}	−3.66°	−0.26°	1.91	8.9×10^{-1}
	838-1-1075-15	6.4×10^{-1}	2.8×10^{-2}	2.3	−0.83°	−0.83°	2.07	5.9×10^{-2}

TABLE 1. Estimates of two sources of error in the velocity records. (i) E_T (see §3.1.1 (iii)) is an upper-bound estimate of possible error in axial velocity spectrum ϕ_{11} due to temperature contamination of the heated-film signal. This estimate is valid for the low-frequency end ($f \approx 1.0$ Hz) of our measurement range; error at higher frequency should be less, due to the nature of the boundary-layer over the heated sensor. (ii) E_w (see §3.2) is an estimate of error in the measured vertical velocity spectrum ϕ_{33} due to anisotropy of the velocity field coupled with an inclination of the submersible-based vertical coordinate from true vertical.

measurements (Grant *et al.* 1962; Nasmyth 1970) and of measurements in the surface mixed layer under waves (Grant *et al.* 1968). However, if the aim is to *investigate* isotropy, one would much prefer a cosine response, i.e. a true axial-speed sensor. It is thus essential to monitor θ and restrict investigations of isotropy to those regions where θ is small. In a totally anisotropic situation where crossflows are near zero, values of $\theta = 5°$, 10° and 15° result in overestimating the true axial mean-square fluctuating component by 1 %, 3 % and 7 % respectively. Requiring $\theta < 10°$ should be an adequate criterion for the investigation of isotropy, since isotropic spectral values for streamwise and cross-stream components differ by $\sim 30\,\%$: this restriction involves little data loss in the present application.

Airfoil probes

Cross-stream velocity components were measured with single-axis airfoil probes (Osborn & Crawford 1980) mounted orthogonally (±5°) 1.8 cm apart, with the 'vertical' (w) and 'horizontal' (v) cross-stream sensors respectively 4.3 and 6.1 cm from the heated-film along the y-axis of the submersible coordinate system (figure 4). The single-axis airfoil consists of a piezoceramic beam mounted in a hollow stainless-steel tube. A soft expoxy nosepiece moulded over this sensing element waterproofs it while still allowing it to bend freely under the aerodynamic lift produced on the probe tip by fluctuating water velocities. When the angle of attack

between probe axis and total velocity is small, output voltage E is related to cross-axis velocity component v, by the linear relationship

$$E = \rho S U v,$$

where ρ is seawater density, U is mean axial flow component ($U \gg v$) and S is an experimentally determined sensitivity. The sensitivity calibration consists of rotating the probe at constant frequency (2.5 Hz) in a submerged water jet of constant speed and measuring r.m.s. output voltage as a function of the angle θ between the probe and jet axes (Osborn & Crawford 1980). This calibration was carried out for each probe both before and after the field work; there was no change in S within experimental error of $\pm 5\%$. Within this same error, the calibrations are linear for $\theta < 15°$ (Gargett 1980).

There is at present no laboratory calibration of the high-wavenumber response of airfoil probes,† a response most properly described in wavenumber space since it is a function of the physical size of the probe rather than an unsteady boundary-layer effect. We have determined the response of the two airfoils used on *Pisces* by fitting to isotropic curves in known isotropic flows: details are provided in the Appendix. All airfoil records are then corrected with this response function. In addition, the airfoil circuits contained a high-pass filter (3 db at 0.5 Hz) originally included to minimize low-frequency temperature-induced effects, rapidly rising and more slowly decaying offsets often observed (Osborn & Crawford 1980) when a probe passes through strong finestructure temperature gradients during vertical free-fall deployments. Such temperature-induced effects are seldom noticed in the present set of measurements, partly because of the small temperature range involved and partly because the probe path is nearly horizontal, while the temperature stratification is dominantly vertical. Thus the effect of this filter is removed in spectral processing. We note that by its nature the airfoil is not a mean-flow sensor, so its response cannot be flat all the way to zero frequency: we do not know the nature of the very-low-frequency response but it is not essential to the measurements reported here.

Rotor current meters

The mean forward speed U of the submersible through the water must be known accurately, since it affects the small-scale velocity measurements in two ways. First, gains of both heated-film and airfoil sensors depend on U, and secondly, U must be used to transform from the time domain of measurement to the spatial domain of theoretical predictions. In addition, measurement of the low-frequency cross-flows V and W are necessary to identify periods when the angle of attack

$$\theta \equiv \sin^{-1}\left(\frac{V^2 + W^2}{U^2 + V^2 + W^2}\right)^{\frac{1}{2}}$$

exceeds limits within which the heated-film acts as an axial-component sensor and the airfoils have linear response. Low-frequency flow components were measured with a set of 3.5 cm diameter ducted rotors developed by Smith (1974). The rotors are mounted in a non-orthogonal triplet so that in steady flow U each rotor senses a substantial component $U\cos(\frac{2}{3})^{\frac{1}{2}}$ of the mean flow, eliminating threshold problems in the cross-component measurements. With small-angle corrections (discussed below),

† This lack has since been remedied by Ninnis (1984), by direct calibration against a laser-Doppler velocimeter: the result is comparable to that given in the Appendix.

each rotor senses the component of flow parallel to the rotor axle. Given the triplet geometry (Gargett 1980), rotor speeds can be combined to yield the components U, V and W of low-frequency flow in the submersible coordinate system (figure 4). Each rotor was calibrated at zero angle of attack to the mean flow in a water tunnel. Points from separate calibrations carried out before and after the cruise agree with 0.1% error in the approximately 0.8 m s^{-1} measured by each rotor at a speed $U \sim 1.0$ m s^{-1}; this stability makes the rotors excellent mean-flow sensors. Small additional errors arise because ducted rotors do not have a perfect cosine response: ours tend to overspeed slightly for the moderate angles of attack typical of submersible operations. We correct for this effect using water-tunnel calibrations of rotor response as a function of θ and an iterative scheme which corrects U, V and W until change in each component is less than 0.1 cm s^{-1}. Since the rotors are not far from a cosine response, and θ is usually small, this rarely takes more than a single iteration. The scale of velocity fluctuations which can be resolved is obviously limited by the size of the triplet rather than the size of the individual rotors. If the underlying turbulent velocity field has an inertial subrange, normalized component 'response functions' can be determined (Kaimal, Wyngaard & Haugen 1968). For the geometry used on *Pisces*, these functions are all 1.0 at wavenumbers $k \lesssim 0.03$ c.p.m. However, at higher k, the axial response falls (to 0.5 at $k \approx 1$ c.p.m.) while both cross-component responses actually rise to broad peaks (of magnitude ~ 1.5 near $k \approx 1$ c.p.m.), before falling steeply at still higher k. Since these response functions depend upon the shape assumed for the velocity spectrum, their usefulness is very limited for the present measurements, which seek to determine that shape. Consequently, we have chosen not to correct the rotor spectra: the uncorrected spectra are used only at wavenumbers less than $k \approx 0.3$ c.p.m., where differences between corrected and uncorrected spectra are less than 10%. When accurate extension to low k is required (§6), we use only the heated-film measurement.

3.2. *Vehicle considerations*

A description of the performance of *Pisces* as a vehicle for turbulent velocity measurements has been given by Gargett (1982). Since the submersible is nearly neutrally buoyant, it responds to fluid motions of scales comparable to its own length and larger: thus our discussion of velocity as measured on the submersible will be confined primarily to scales smaller than this ($\lesssim 10$ m). We are concerned with features of the vehicle which affect accuracy and/or interpretation of velocity data, namely:

(1) effect of non-zero angle between the submersible coordinate system to which measured velocities are referred (figure 4) and a geographical coordinate system in which vertical is the direction of (local) gravity;

(2) possible flow modification due to the presence of a vehicle;

(3) magnitude and variability of velocity 'noise' induced by vehicle vibration.

The first point is of no concern if turbulence is isotropic at all measured scales; however, if we wish to investigate the effects of stratification, it becomes essential to distinguish true vertical, since this is the direction in which work is done, either against gravity in initial overturning stages of turbulence, or possibly by gravity in the collapse of partially mixed remnants of such events. Figure 6 sketches the coordinate systems involved, here simplified to two dimensions. The local geographic coordinate system (x, z) is not necessarily coincident with one (p, n) aligned locally parallel and normal to isopycnals: for the reason outlined above, the former is the fundamental one. The direction of motion of the submersible's centre of mass makes

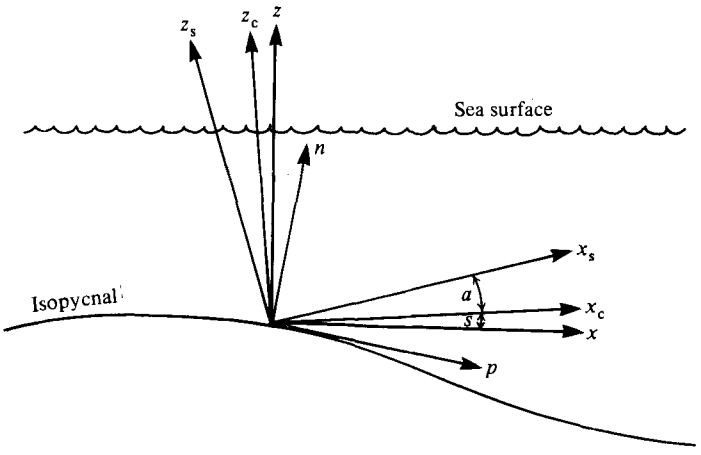

FIGURE 6. Coordinate systems of importance to submersible-based velocity measurements: for discussion see §3.2. (x, z) geographic coordinates with z = local vertical; (x_c, z_c) submersible centre-of-mass coordinates; (x_s, z_s) coordinates of velocity measurements; (p, n) coordinates parallel and normal to isopycnals.

an angle s with x, defining coordinates (x_c, z_c), while the measurement coordinate system (x_s, z_s) attached to the submersible may be rotated a further angle a from (x_c, z_c). If (u, w) and (u_T, w_T) are velocity components measured in the submersible and geographic coordinates respectively, then mean-square velocities are related (in the small-angle approximation $a+s \ll 1$ rad) by

$$\overline{u_T^2} = \overline{u^2} + \overline{w^2}(a+s)^2 = \overline{u^2}(1+e_u),$$
$$\overline{w_T^2} = \overline{w^2} + \overline{u^2}(a+s)^2 = \overline{w^2}(1+e_w),$$

provided $\overline{uw} = 0$. The fractional errors involved in assuming that $\overline{u^2} = \overline{u_T^2}$ and $\overline{w^2} = \overline{w_T^2}$ are respectively

$$e_u = \frac{\overline{w^2}}{\overline{u^2}}(a+s)^2, \quad e_w = \frac{\overline{u^2}}{\overline{w^2}}(a+s)^2:$$

these are systematic errors by which true values are overestimated. If turbulence is isotropic, i.e. $\overline{u_T^2} = \overline{w_T^2}$, both velocity components are overestimated by the same amount, hence the velocity *ratio* $\overline{w^2}/\overline{u^2}$ is correct. However, if stratified turbulence decays by preferentially extracting energy from the vertical component, as commonly supposed, one might imagine a limit where $w_T \to 0$ but $u_T \neq 0$. In this case, $e_u \to 0$, but $e_w \to \infty$: that is, as $\overline{w_T^2} \to 0$, measured $\overline{w^2}$ becomes totally an artifact of any inclination of the submersible-based coordinate system to true horizontal.

To determine the magnitude of this effect, we have estimated e_w for each of the records used in this paper. Path angle s is calculated as $s = \sin^{-1}(\Delta z/\overline{U}\Delta t)$, where Δz(m) is the difference in depth between beginning and end of the record, $\overline{U}$ (m s^{-1}) is mean forward speed measured by the rotor triplet (this is not exactly the centre-of-mass velocity $\boldsymbol{u}_c$, but the difference is insignificant in this calculation) over the time extent Δt(s) of the record. Attitude angle a is estimated as

$$a = \sin^{-1}\frac{\overline{W}}{(\overline{U^2}+\overline{W^2})^{\frac{1}{2}}},$$

using rotor speeds $(\overline{U}, \overline{W})$ measured in the submersible coordinate system averaged over the record length. As a measure of $\overline{u^2}/\overline{w^2}$, we have used the ratio of measured

horizontal to vertical velocity spectral densities at the lowest wavenumber ($k \sim 0.5$ c.p.m.) of standard processing (see §3.4). The resulting values of e_w (table 1) indicate that over the range of angles involved in normal submersible operations and the range of spectral intensities observed, measurements of vertical velocity in the submersible-based coordinate system can be interpreted as true vertical velocity with less than 2% error due to contamination by horizontal velocity.

The second question is that of upstream influence of the vehicle at the location of the high-frequency sensors. As a mean flow approaches an obstacle, it must diverge to pass around it. As an obstacle, *Pisces* is considerably narrower than it is high ($\sim 1:3$): this aspect ratio and the constraint of vertical stratification make it easier (energetically) for water to pass around the vehicle in a horizontal rather than vertical plane. Thus we expect that flow around *Pisces* is better modelled by flow past a circular cylinder (of radius $r \approx 1$ m equal to that of the personnel sphere) rather than by flow around a sphere. Distortion of turbulence by a circular cylinder has been studied in the laboratory by Britter, Hunt & Mumford (1979). By $x = 4r$, a distance of four radii from the centre of a cylinder along the stagnation streamline, they find that the only significant effect is a reduction of the mean flow by $\sim 7\%$ from its upstream value (which, significantly, is taken as the value at $x = 5r$). Root-mean-square turbulent intensities and spectral shapes are significantly affected only for values of $x \lesssim 3r$. Since the high-frequency sensors on *Pisces* were at a distance of $\sim 4r$ from the centre of the personnel sphere, the turbulent velocity measurements should be free of vehicle-induced contamination. Since the probe location is actually below the sphere centreline, oncoming flow sees an obstacle of smaller radius; any mean speed reduction should be smaller than the 7% quoted above, and thus U has not been corrected for vehicle effects.

Finally, be it towed or self-propelled, any vehicle that moves horizontally vibrates, producing an effective noise level for velocity measurements. *Pisces* vibrational noise is dominated by the fundamental frequency of its driving propellers and by various higher harmonics which appear as narrow peaks in the measured velocity spectra (Gargett 1982). Figure 7 presents spectra of component velocities as a function of frequency for three 'noise' records (defined simply as the lowest levels observed). The heated-film measurement of $u(HF_u)$ overlaps that of the rotor triplet (R_u) at low frequency. These two traces diverge above $f \approx 0.3$ Hz as a result of the unknown spatial response of the triplet: we use 0.3 Hz as the upper limit of resolution of all rotor-derived velocity components. The position of the fundamental vibration frequency (1) and higher harmonics (2–7) are shown along the scale in the upper right. Although the vibration-induced velocity peaks are extremely narrow-band (Gargett 1982), they are broadened in this representation by the logarithmic-bandwidth averaging used in standard spectral processing of velocity records (§3.4). While vibrational contamination of the submersible velocity records is not negligible, it has the attractive feature of constancy. Over the frequency range of interest, observed noise levels do not vary significantly provided *Pisces* is run with full power to both thrusters. This feature allows use of some small multiple of the upper bounds of the spectra shown in figure 7 as an operational criterion for determining vibrational contamination of observed velocity spectra.

3.3. *Estimation of buoyancy frequency*

The Brunt–Väisälä or buoyancy frequency N is a primary measure of stability in a stably stratified fluid. As such it is an essential parameter if the present results, taken in a highly stable but also highly dissipative system, are to be applied to the lower

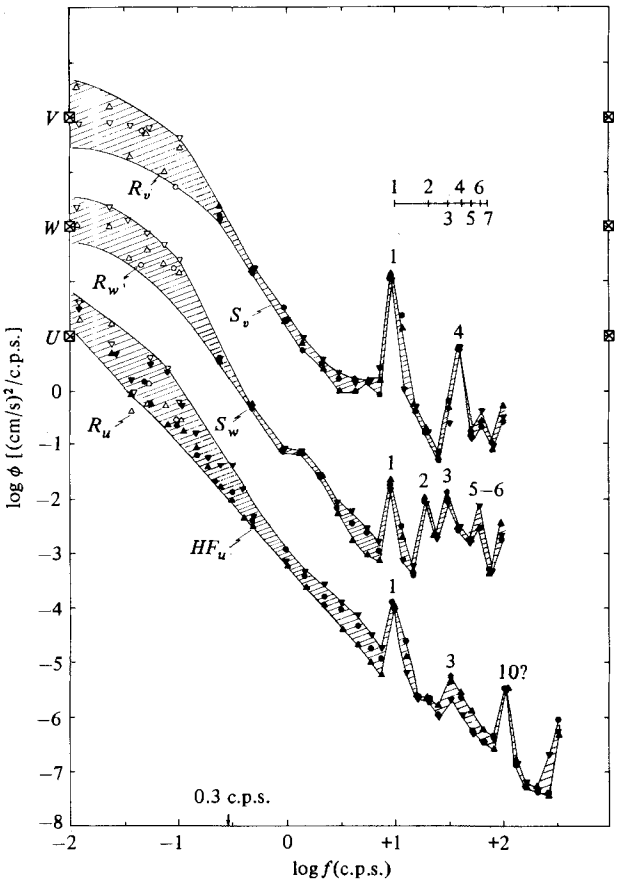

FIGURE 7. Noise-level velocity component spectra for the submersible measurements. The vertical scale is correct for the u-component spectrum, while cross-component spectra are each shifted up two divisions for ease of inspection. Solid symbols are measured from the heated-film (HF_u) and the two cross-axis airfoil probes (S_w and S_v), while open symbols are from the rotor-triplet determination of u, v and w (R_u, R_v, R_w). Well-defined spectral peaks due to vibration-induced velocities are found at the fundamental frequency (1) of the submersible's propellors and at a number of higher harmonics (positions noted at top right). The observed constancy of motional noise levels allows us to use some small factor times the upper bound of these curves to assess possible vibrational contamination of measured spectra.

stabilities and lower dissipation rates characteristic of the ocean. Unfortunately, since N involves the vertical derivative of density, it is not a particularly easy parameter to measure from a near-horizontal measurement path. We are nevertheless forced to attempt to estimate N from parameters measured on *Pisces* because simultaneous vertical CTD profiles were not possible, both because of constraints associated with manned submersible operations and, more seriously, because lateral structure of the wave forms with which turbulence was associated required that the gradient measurement be made right at the submersible. All we have to work with is a measurement of T and S at one point, and a difference temperature ΔT over a distance $\Delta z = 0.8$ m above this point. However, because of the deformation of density surfaces associated with the large-scale waveforms of both flow regimes, the single-point (T, S)-measurement along a near-constant depth is converted into the slope $m = \Delta T/\Delta S = T_z/S_z$ of the local (T, S)-curve, as seen in figure 8. Two points should be

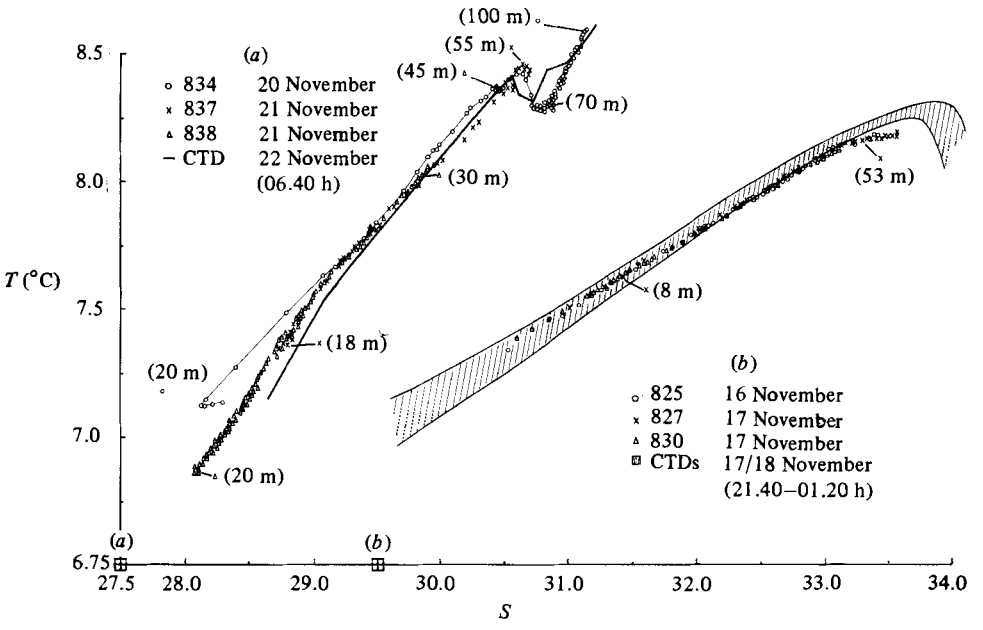

FIGURE 8. A comparison of (T, S)-curves measured from a vertically profiling CTD and from the horizontally moving sensors on *Pisces*. In regimes of large isopycnal displacements, such as those in Knight Inlet, horizontal measurements yield the local (T, S)-slope as isopycnals move up and down past the measurement depth. Adding a vertical difference temperature measurement from *Pisces*, this local slope can be used to estimate the local value of N (§3.3). Given the rapid change in (T, S)-characteristics with time (figure 2), this comparison is presented only for Pisces measurements taken within $\sim$ 24 h of available CTD casts: (*a*) for the separated boundary-layer flow to the west of the sill the single CTD available is shown as a heavy line; (*b*) for the internal wavetrain the ensemble of CTD casts to the east of the sill is shown as the shaded region. The salinity scale is correct for case (*a*): case (*b*) has been shifted to the right by 2.0.

remarked. First, this slope is a *local* characteristic in both space and time. The (T, S)-slope measured from *Pisces* is distinctly different east and west of the sill, in agreement with (T, S)-characteristics determined from vertical CTD profiles taken with 24 hours of the submersible measurements. (T, S)-slopes determined from *Pisces* during the period between the two sets of CTD stations discussed in §2 show slopes intermediate between the extremes of figure 2. Second, in the upper waters of the inlet, the local (T/S)-relation is *extremely* linear, a consequence (one may here be sure) of vigorous turbulent mixing between an upper cool fresh water type and a warmer saltier deep water. We estimate a possible error of $\sim 10\,\%$ in determination of m by comparing the observed slope in figure 8(*b*) to the mean slope derived from the ensemble of CTD observations to the east of the sill. This may overestimate the error, since some of the difference is probably due to the small but finite differences between the two measurements.

Assuming a linear equation of state, and ignoring the effect of compressibility for our shallow measurements, we may write

$$N(\text{rad s}^{-1}) = -\left(\frac{g\rho_z}{\rho_0}\right)^{\frac{1}{2}} = (g(\alpha T_z - \beta S_z))^{\frac{1}{2}} = \left(g\left(\alpha - \frac{\beta}{m}\right)T_z\right)^{\frac{1}{2}},$$

where $g = 9.81$ m s^{-2} is the acceleration due to gravity, $\alpha \equiv -(1/\rho_0)\,\partial\rho/\partial T\,(°\text{C})^{-1}$ and $\beta \equiv (1/\rho_0)\,\partial\rho/\partial S\,(\text{nsu})^{-1}$ are thermal and saline expansion coefficients for seawater (Neumann & Pierson 1966), and T_z(°C/m) is the vertical temperature gradient ($T_z < 0$

Class	Record	$\frac{\Delta T}{\Delta z}$ (°C/m)	m	N (rad s^{-1})	N (c.p.h.)	ϵ_1 (m^2 s^{-3})	$k_s \equiv (\epsilon_1 \nu^3)^{\frac{1}{4}}$ (rad m^{-1})	$k_b \equiv (N^3 \epsilon_1^{-1})^{\frac{1}{2}}$ (rad m^{-1})	l_b (m)	$I \equiv \frac{k_s}{k_b}$
1	822-1-1030-19	—	—	—	—	4.7×10^{-6}	1.1×10^{3}	—	—	—
	825-2-2350-12	6.5×10^{-2}	0.30	1.9×10^{-2}	11	1.8×10^{-5}	1.5×10^{3}	6.2×10^{-1}	10	2400
	825-2-2725-18	6.1×10^{-2}	0.30	1.6×10^{-2}	9	2.1×10^{-5}	1.6×10^{3}	4.4×10^{-1}	14	3600
	825-2-3150-10	6.6×10^{-2}	0.30	2.0×10^{-2}	12	3.8×10^{-5}	1.9×10^{3}	4.6×10^{-1}	14	4100
2	832-1-4000-20	5.9×10^{-2}	0.46	1.1×10^{-2}	6	9.5×10^{-7}	7.4×10^{2}	1.2	5.2	620
	826-3-4500-42	6.1×10^{-2}	0.30	1.6×10^{-2}	9	3.5×10^{-6}	1.0×10^{3}	1.1	5.7	910
	839-1-3050-29	8.5×10^{-2}	0.62	2.1×10^{-2}	12	3.6×10^{-6}	1.0×10^{3}	1.6	3.9	630
	831-1-4760- 9	8.0×10^{-2}	0.56	2.1×10^{-2}	12	5.9×10^{-6}	1.2×10^{3}	1.3	4.8	920
3	831-2-2355-23	1.7×10^{-1}	0.56	4.2×10^{-2}	24	4.1×10^{-6}	1.1×10^{3}	4.3	1.5	260
	831-1-3925-41	8.4×10^{-2}	0.56	2.2×10^{-2}	13	1.3×10^{-6}	8.0×10^{2}	2.9	2.2	280
	832-1-4975-24	5.9×10^{-2}	0.46	1.1×10^{-2}	6	3.2×10^{-7}	5.6×10^{2}	2.0	3.1	280
	837-2-4100-15	9.0×10^{-2}	0.55	2.4×10^{-2}	14	9.7×10^{-7}	7.4×10^{2}	3.8	1.7	190
4	838-1- 220-23	7.4×10^{-2}	0.64	1.7×10^{-2}	10	1.8×10^{-7}	4.9×10^{2}	5.2	1.2	94
	825-1-3400-29	1.0×10^{-1}	0.32	3.8×10^{-2}	22	4.9×10^{-7}	6.2×10^{2}	11.0	0.57	56
	831-2- 150-42	8.5×10^{-2}	0.56	2.2×10^{-2}	13	1.9×10^{-7}	4.9×10^{2}	7.5	0.84	65
	838-1-1015-15	2.1×10^{-1}	0.64	4.6×10^{-2}	26	1.3×10^{-6}	8.0×10^{2}	8.7	0.72	92

TABLE 2. Values of various derived parameters for the velocity records considered in §§4 and 5, arranged by class. Vertical temperature gradient $\Delta T/\Delta z$ and slope m of the local (T, S)-relation as measured in *Pisces* are used to estimate the local value of buoyancy frequency N associated with each record (for details see §3.3). The turbulent kinetic energy dissipation rate ϵ_1 is calculated from integration of the well-resolved axial-velocity-component dissipation spectrum, assuming dissipation-scale isotropy (equation (14), §4). It is used to calculate the Kolmogoroff wavenumber $k_s \equiv (\epsilon_1 \nu^{-3})^{\frac{1}{4}}$ (where $\nu = 1.48 \times 10^{-6}$ m^2 s^{-1}, the kinematic viscosity of seawater at 8 °C) and buoyancy wavenumber $k_b \equiv (N^3 \epsilon_1^{-1})^{\frac{1}{2}}$ for each record. The final column is the ratio $I \equiv k_s/k_b$, a useful parameter in classifying the behaviour of velocity component spectra during decay (indeed the basis for the classes shown in the first column).

for these measurements). To provide the estimates of N used in the remainder of this paper (table 2), we calculate the above expression with measured values of m and the approximation $T_z \approx (\Delta T - \Delta_0)/0.8$ (°C/m), where $\Delta T = \overline{T_B} - \overline{T_A}$ is the difference between temperatures as measured by the A and B thermistors (the overbar denotes an average over the record length used for the velocity analysis). The offset Δ_0 arises because the heavily averaged temperature measurements are precise but not particularly accurate since the thermistors were not calibrated in different mode. This offset must be determined and removed before calculating N. We have determined Δ_0 from an average value of $(\Delta T)_0 = (0.0500 \pm 0.0004)$ °C from several hundred metres of records deep in the inlet at a time when CTD measurements gave $(T_z)_0 = (2\text{–}4) \times 10^{-3}$ °C/m. Using the midpoint of this range, we calculate $\Delta_0 = 0.0524$ °C $\pm 2\,\%$, where the error is from estimation of $(\Delta T)_0$ and the spread in $(T_z)_0$. Errors in T_z range from 0.5 % for the largest (0.21 °C/m) to a maximum of 13 % for the smallest (0.0078 °C/m) calculated gradients. Using our (over)estimated error of 10 % in m, the error in N is thus a maximum of 5 % (11 %) for the largest (smallest) values encountered.

3.4. *Selection and processing of data*

Although the *Pisces* system collected a vast amount of data, a much more limited amount satisfied all the criteria that we wish to meet for the present analyses, namely all velocity sensors operating, no plankton spikes or course alterations, less than 10 cm s^{-1} discrepancy between hot-film and rotor mean speeds, and small contamination due to temperature and/or angle effects. Records that satisfied these requirements received standard processing. The high-resolution velocity signals were broken into blocks of fixed length corresponding to 4.096 s of time, or ~ 4 m of distance. Each block was first-differenced and cosine-tapered over the first and last 5 % of the block, then raw power-spectral densities were calculated using the FFT technique. Raw estimates were block-averaged over the number M of such blocks in a record, then corrected for first differencing and for loss of variance due to the cosine taper. Resulting values were further band-averaged in frequency with logarithmically increasing bandwidth, then finally corrected for probe and filter responses and gains. The velocity spectra are extended to lower wavenumber using rotor-derived components below 0.3 Hz: however, possible contamination of low-wavenumber spectral values by interaction between submersible and flow must be kept in mind.

In all plots and tables, records are identified by Tape-File-Starting block-M (see also the caption to figure 5*a*). Tapes 837–839 were recorded west of the sill on 21 November, while all remaining tapes were recorded east of the sill on 15 November (tape 822), 16 November (tapes 825–826), and 19 November (tapes 831–832). Statistical confidence limits can be calculated for each record (assuming that each frequency estimate is independent) and compared with actual error bars calculated from the variance of estimates at a single frequency. A comparison for two records with $M = 10$ and 19 respectively is shown in figure 9(*a*). Since the two estimates agree well, we choose to indicate the maximum statistical error in each class of spectra by plotting theoretical error bars for the record with the smallest number of edof (M): error bars for other records in the class will be smaller, often substantially.

The averaged corrected spectra are first plotted as a function of frequency for comparison with the appropriate noise level spectra (cf. figure 9*a*): values less than three times the noise level at the same frequency are flagged and removed from further analysis. Spectra are then converted from the frequency domain of

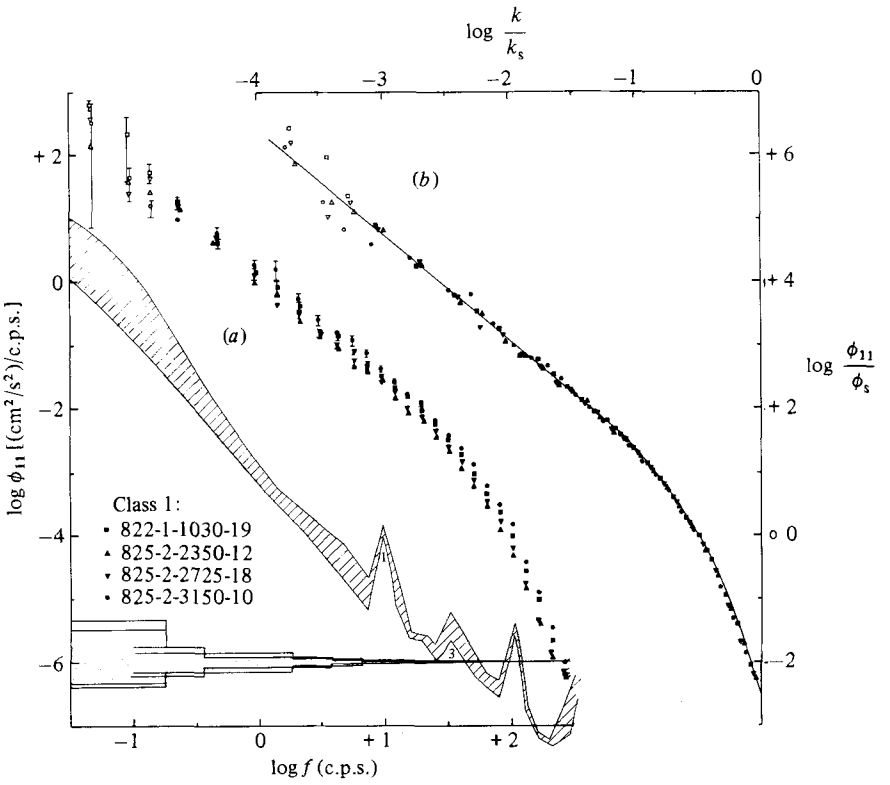

FIGURE 9. (*a*) Dimensional plots of ϕ_{11}, the u-component spectrum as a function of frequency for Class 1 records. Solid and open symbols denote respectively results from heated-film and rotor triplet measurements of u. Records are identified by Tape-File-Starting block-M, where M is the number of independent sample blocks averaged at the lowest wavenumber estimate of the solid symbols. Estimates of 95% confidence limits for records with the largest and smallest number of degrees of freedom are plotted at the bottom of this figure. Actual error bars calculated from variances of estimates at a single frequency are shown for these same two records. The two estimates are comparable, and both are smaller than plotted symbols at frequencies above ~ 10 c.p.s. The shaded region is the observed range of noise spectra (figure 7). (*b*) The spectra of (*a*) converted to wavenumber space by the Taylor hypothesis, then non-dimensionalized by Kolmogoroff scales ϕ_s and k_s. The solid curve is a 'universal' curve derived from these data (§4).

measurement to the wavenumber domain of theory using Taylor's hypothesis $\partial/\partial t = -U\partial/\partial x$, valid if $u'/U \ll 1$, where U is the velocity of the vehicle relative to the fluid and u' is an r.m.s. velocity of the energy-containing scales of the turbulence. Unfortunately, owing to the vehicle-motion problem at low wavenumber, it is often difficult to determine u' from the *Pisces* measurements. However, it will be suggested later (§6) that typical values of $u' \sim (1\text{–}2)\,u_b$. From this relation and the values of ϵ and N given in table 2, it appears that maximum turbulent intensities (those of Class 1 records) are of order $u'/U \sim 0.06$, not much higher than flows for which the Taylor hypothesis has been verified directly (Champagne *et al.* 1970).

Measured spectra are non-dimensionalized for comparison with the local similarity forms of (6) and (8) using the Kolmogoroff scales $\phi_s \equiv (\epsilon_1 \nu^5)^{\frac{1}{4}}$ and k_s, both calculated using the isotropic value

$$\epsilon_1 \equiv 15\nu \int_0^\infty k^2 \phi_{11}(k)\,\mathrm{d}k = 15\nu \sum_{j=1}^{p} k_j^2\, \phi_{11}(k_j)\,\Delta k_j \tag{14}$$

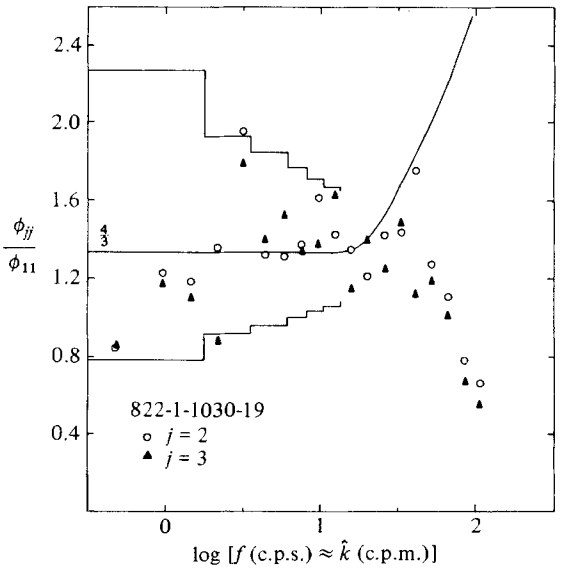

FIGURE 10. Ratios of cross-stream/streamwise velocity component spectra as a function of frequency (wavenumber) for record 822-1-1030-19. Measured values lie within statistical error bounds for over a decade in wavenumber, much stronger evidence of isotropy than the $-\frac{5}{3}$ slope of $\phi_{11}(k)$. The high-frequency (wavenumber) roll-off of the ratios, due to finite size of the airfoil probes, can be corrected by a response function determined from records, such as this, which exhibit evidence of isotropy before the scales affected by probe size (see Appendix). Subsequent presentations of cross-stream spectra include this response correction.

determined from the axial-component spectrum, with $\nu = 1.48 \times 10^{-6}$ m^2 s^{-1}, valid for the restricted temperature range in Knight Inlet. This is our primary measurement of ϵ, since the entire response of the heated-film system is known and since vibration-induced noise is a minimum in this component. The only vibrational peak that sometimes affects determination of ϵ is the one at $f = 106$ Hz. For records which show a peak in the dissipation spectrum at 106 Hz, the peak value was replaced by an average of the neighbouring spectral estimates before ϵ_1 was calculated: because the 106 Hz peak is always well above the broad peak of the dissipation spectrum, the error involved in such a correction is negligible. The endpoint of the integration in (14) was taken as the point k_p at which $k^2\phi_{11}(k)$ began to rise monotonically at high wavenumber.

4. Class 1 spectra: $I \sim 3000$

Class 1 records, all from the first one or two waves of the internal wavetrain, exhibit many of the characteristics that follow from Kolmogoroff's first two hypotheses (similarity under scaling with ϵ and ν and $-\frac{5}{3}$ subranges) as well as satisfying the condition (4) for local isotropy. Dimensional plots of ϕ_{11} for four such records (figure 9*a*) indicate that only the highest measured frequency needs be rejected on the basis of noise. Kolmogoroff scaling produces a very well-defined curve (figure 9*b*) at non-dimensional wavenumbers larger than $k/k_s \approx 10^{-1.5}$. At lower wavenumbers there is progressively more scatter about a line of $-\frac{5}{3}$ slope, presumably the result of submersible motions. The ratios ϕ_{22}/ϕ_{11} and ϕ_{33}/ϕ_{11} are equal and exhibit at least one, sometimes two, decades of the isotropic $\frac{4}{3}$ value (shown for one record in figure

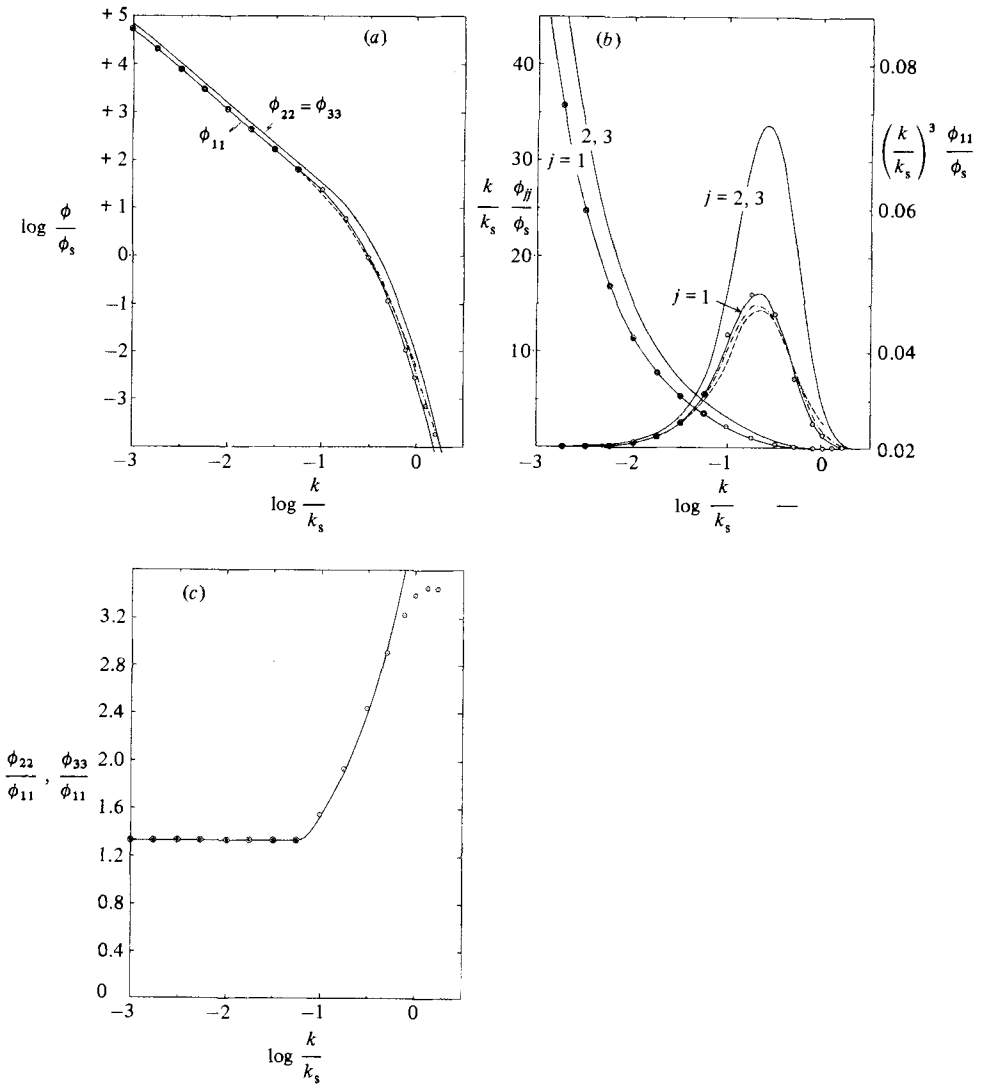

FIGURE 11. A comparison of 'universal' spectra for high Reynolds number turbulence: ——, Grant *et al.* (1962); ⊙——⊙, Nasmyth (1970); —·—, Champagne (1978); —, present data at high wavenumbers, with double-circled points at low wavenumbers. (*a*) Classic log/log format of the energy spectra. (*b*) Variance-preserving forms of energy and dissipation spectra for streamwise ($j = 1$) and cross-stream ($j = 2, 3$) components. (*c*) Cross-stream/streamwise spectral ratios: circled points are derived from the Nasmyth (1970) spectrum for $\phi_{11}(k)$ (Oakey 1982).

10) before falling at high wavenumber because of the (unknown) high-wavenumber roll-off of the airfoils (§3.1). Clearly this response must be determined if we are to examine possible changes in the high-wavenumber velocity spectra as turbulence decays. Lacking a laboratory calibration of response (at the time this paper was first written), we determined airfoil spectral response by requiring that airfoil spectra match the high-wavenumber form predicted by (4), where $\phi_{11}(k)$ is the 'universal' form determined from the heated-film spectra for these Class 1 records: achievement of the $\frac{4}{3}$ ratio for a decade before the probe response becomes significant assures that this is an appropriate procedure. Details of the response determination are outlined

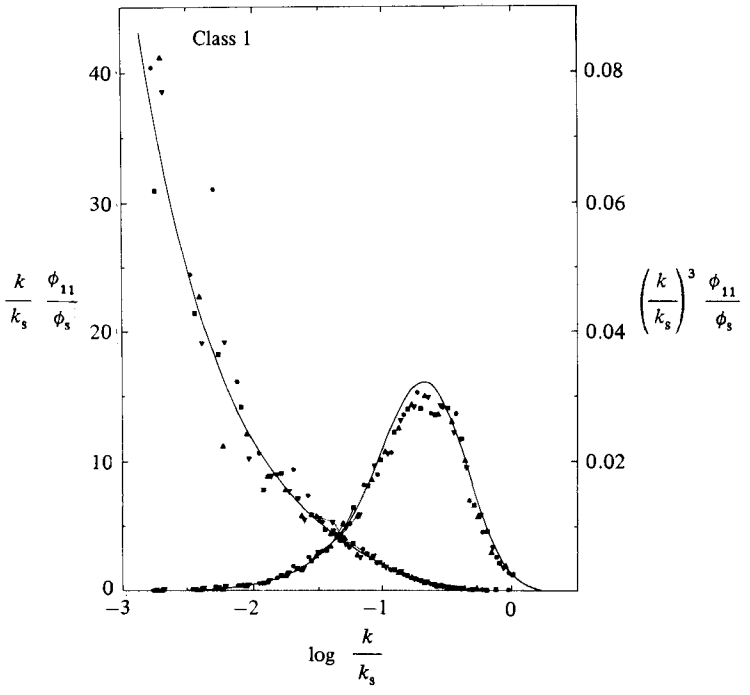

FIGURE 12. Variance-preserving energy and dissipation spectra for the stream-wise velocity spectra of figure 9. The estimate (14) of the kinetic-energy dissipation rate used in the Kolmogoroff variables,

$$\phi_s \equiv (\epsilon_1 \nu^5)^{\frac{1}{4}}\ \mathrm{cm^2\ s^{-2}/(rad\ m^{-1})} \quad \text{and} \quad k_s \equiv (\epsilon_1/\nu^3)^{\frac{1}{4}}\ \mathrm{rad\ m^{-1}},$$

is proportional to the area under this dissipation curve, which is completely resolved by the heated-film measurement.

in the Appendix, and any further presentations of cross-component spectra have been corrected for this response.

The first observational determination of the Kolmogoroff 'universal' spectral shape for wavenumbers above the $k^{-\frac{5}{3}}$ inertial subrange was that of Grant *et al.* (1962); however, they pointed to obvious effects of noise at the highest wavenumbers. Lower noise levels were achieved by Nasmyth (1970)† and by Champagne (1978). While the inertial subrange is well-established by these measurements, there are small differences in high-wavenumber shapes (figure 11): thus we chose to generate independent 'universal' curves using the data of figure 9 to determine ϕ_{11}/ϕ_s at high wavenumbers ($10^{-1.25} \leqslant k/k_s \leqslant 1$), then calculating ϕ_{jj}/ϕ_s from (4). Shown as the solid curve of figure 11(*a*), our fit of the streamwise spectrum differs most significantly from the others by a slightly steeper roll-off at the highest wavenumbers.

The degree to which data fit a 'universal' curve is most evident in the variance-preserving form of the dissipation spectrum shown in figure 11(*b*), where small differences in the 'universal' form for ϕ_{11}/ϕ_s due to differences in curve-fitting procedures are amplified when multiplied by $(k/k_s)^3$. Figure 12 shows such a plot for the Class 1 spectra: our functional form is slightly higher ($\sim 3\,\%$) than the data over

† Oakey (1982) has recently documented Nasmyth's values for $\phi_{11}(k)$ and derived associated values for $\phi_{22}(k)$ using (4): in any comparisons between Oakey (1982) and this paper beware a factor 2π introduced by Oakey in the definition of the universal functions: in the present paper, wavenumber k has units of rad m^{-1}, not c.p.m.

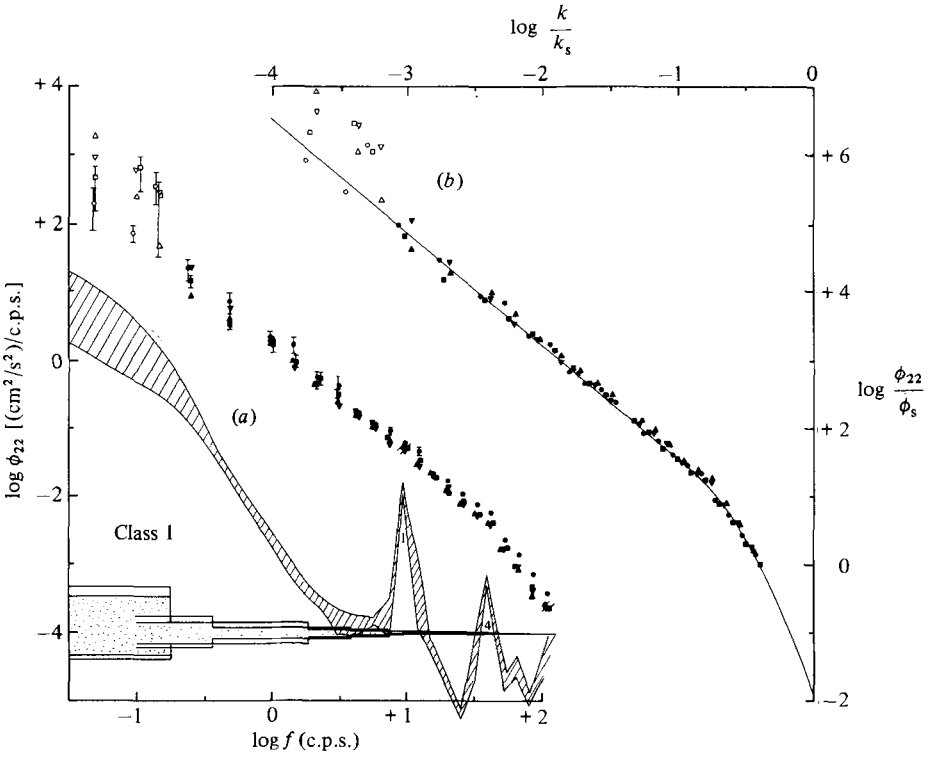

FIGURE 13. (*a*) Dimensional plots of ϕ_{22}, the v-component cross-stream spectrum as a function of frequency for Class 1 records. Solid and open symbols denote respectively results from airfoil probe and rotor triplet measurements of v. Flagged points (less than 3 times the upper noise level spectrum) are removed from further analysis. (*b*) Spectra non-dimensionalized by Kolmogoroff scales ϕ_s and k_s.

the spectral peak, an indication of the size of error involved in curve fitting (this error will obviously propagate into the universal form for ϕ_{22}). Deviations from the universal dissipation spectrum will have to be much larger than the discrepancy shown in figure 12 before being accepted as evidence of anisotropy at dissipation scales. Figure 12 also presents the variance-preserving energy spectrum: scatter at low wavenumbers we attribute to vehicle motion.

For completeness, we present in figures 13 and 14 respectively spectra of $\phi_{22}(k)$ and $\phi_{33}(k)$, both (*a*) in dimensional units to establish signal-to-noise ratios and point out those vibrational peaks which are troublesome, and (*b*) non-dimensionalized by ν and ϵ_1 to compare with universal curves. From figure 13 (*a*) it is obvious that ϕ_{22} will almost always be noise-contaminated at the fundamental vibration frequency (1). For these records, this frequency lies above the major variance in the energy spectrum and below the major variance in the dissipation spectrum, hence has minor effect. The fourth harmonic (4) has more serious potential for contaminating dissipation spectra, as will be seen in §5. The vertical velocity spectra ϕ_{33} lie well above noise at all except the highest frequency (figure 14*a*), and collapse more nearly to a universal curve than do ϕ_{22}, a result of the lower vibrational peaks in this direction. In the following sections, we consider ϕ_{33} as the more reliable cross-component measurement at high wavenumbers.

Variance-preserving plots of the cross-stream energy and dissipation spectra are

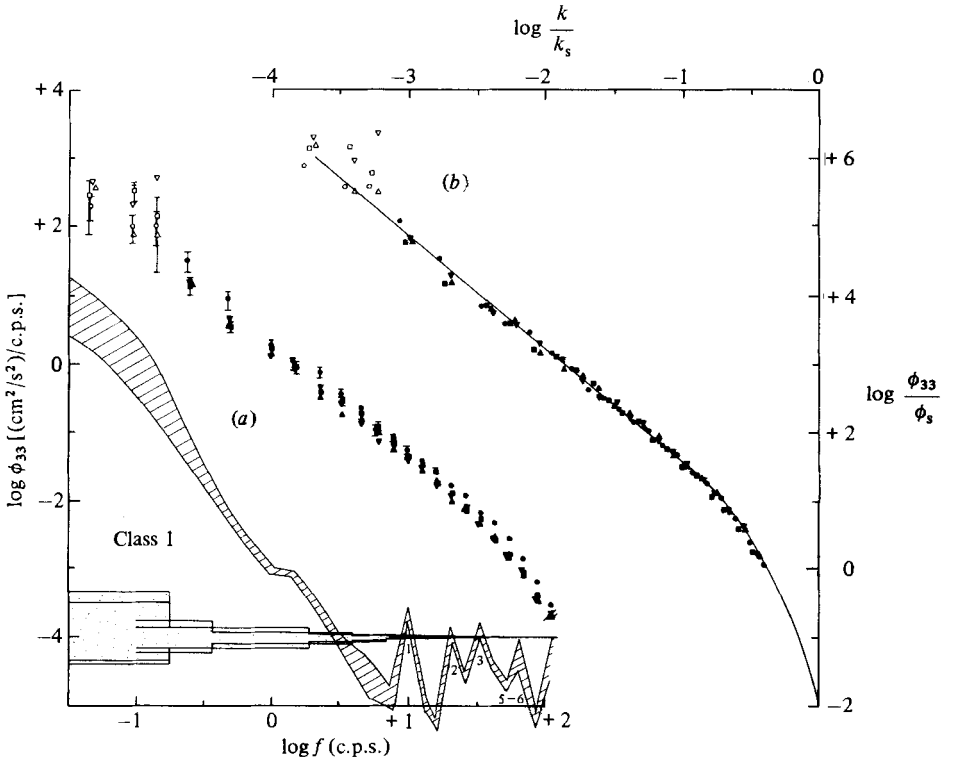

FIGURE 14. (*a*) Dimensional plots of ϕ_{33}, the w-component cross-stream spectrum as a function of frequency for Class 1 records. Solid and open symbols denote respectively results from airfoil probe and rotor-triplet measurements of w. Flagged points (less than 3 times the upper noise level spectrum) are removed from further analysis. (*b*) Spectra non-dimensionalized by Kolmogoroff scales ϕ_s and k_s.

shown in figure 15. Spread of the data about the peak of the dissipation spectrum is partly due to the effects of vibration in the cross-stream directions and possibly partly because data from both cross-stream channels were averaged to determine a single airfoil response function (see the Appendix). The fact that $\phi_{22} > \phi_{33}$ rather consistently near the peak of the dissipation spectrum (see also figures 13*b*, 14*b*) suggest that individual airfoils may have slightly different response functions. Noise levels in both cross-stream components prevent resolution of their dissipation curves much past the peak.

Finally, figure 16 shows spectral ratios, ensemble-averaged over the four isotropic records to increase the edof of the lowest three estimates. Error bars about a value of $\frac{4}{3}$ are calculated from Fisher's F-distribution (Jenkins & Watts 1968). Differences between data and the universal ratio curve in the region where the curve begins to rise are significant: they may be accounted for by slight differences between measured and fitted ϕ_{11}, as discussed in connection with figure 12, and/or by error in determination of the airfoil response correction, as discussed in the Appendix.

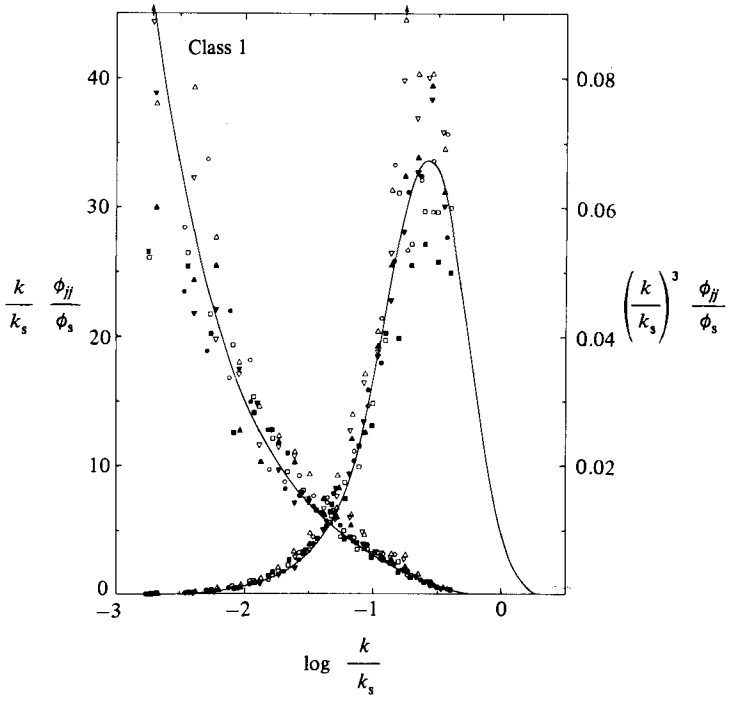

FIGURE 15. Variance-preserving plots of energy and dissipation spectra of the v (open symbols) and w (solid symbols) cross-component spectra of figures 13 and 14. Noise levels in these spectra are sufficiently large that the roll-off region of their dissipation curve is not well delineated, although the beginning of the descent from a peak is seen in all the w-component dissipation spectra (w is less affected by noise than v).

5. The retreat from isotropy

The present measurements indicate that turbulence in a stratified fluid achieves sizeable inertial subranges only in regions of strong forcing. The Class 1 records of §4 come from the leading one or two waves of the internal wavetrain, where echo-soundings show 'turbulence' occupying $\sim$ 10 m in the vertical. (On the basis of the echo-sounding records, the region near the point of boundary layer separation near the sill may also produce turbulence that is locally inertial over a wide range of scales.) Elsewhere the echo soundings show more limited vertical extent, as turbulence is inhibited by the stable stratification. Through the range of conditions encountered in Knight Inlet, we find that the behaviour of measured spectral shapes and ratios is well classified by the parameter I defined by (13). The isotropic and locally inertial records of §4 are characterized by $I \gtrsim 3000$ (table 2), the maximum values observed. Thus k_b lies at least three decades in wavenumber below the wavenumber k_s by which velocity gradients have been wiped out by molecular diffusion: apparently this is sufficient 'room' in wavenumber space for development of an inertial cascade. All other records have lower I-values. From these, we will discuss three classes of records characterized by specific ranges of I and by different spectral shapes. Although we have chosen specific stages, it should be emphasized that evolution is continuous between stages.

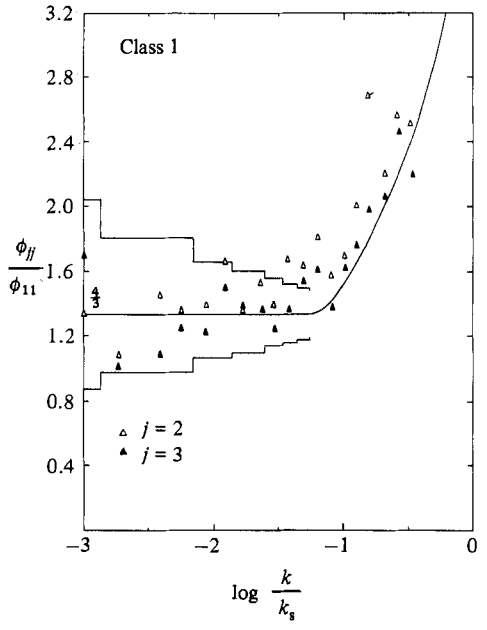

FIGURE 16. Ratios of cross-stream/streamwise velocity components, ensemble-averaged over the spectra of figures 9, 13 and 14. Open symbols are ϕ_{22}/ϕ_{11} and closed symbols are ϕ_{33}/ϕ_{11}. Observed ratio values are within the expected statistical error of $\frac{4}{3}$ over approximately two decades in wavenumber, then rise at higher wavenumbers with the universal ratio curve. The flagged point of ϕ_{22}/ϕ_{11} appears to be slightly affected by uncorrected noise in ϕ_{22} at the 5th harmonic of the fundamental vibration frequency.

5.1. *Class 2 records*: $600 < I < 900$

Records in Class 2 have been chosen to illustrate the point just mentioned, that although we can identify particular stages in turbulent decay when spectra take on distinctive shapes, the evolution between these stages is continuous. The previous Class 1 spectra had clear $-\frac{5}{3}$ subranges in all spectral components: the following Class 3 spectra will show clear -1 subranges in the cross-stream components and a slight droop of $\phi_{11}(k)$ below the $-\frac{5}{3}$ line at the lowest wavenumbers. The Class 2 spectra span these extremes.

Dimensional and non-dimensional component spectra of the Class 2 records are shown in figures 17 (ϕ_{11}) and 18 (ϕ_{33}): $\phi_{22} \approx \phi_{33}$ within statistical error bounds. Dimensional spectral levels are considerably lower than the Class 1 records, leading to more frequent rejection of spectral estimates. Within statistical error, the ϕ_{11} spectra (figure 17) maintain the $-\frac{5}{3}$ dependence of the Class 1 records: the only possible exception is the lowest wavenumber estimate from the heated film in 831-1-4760, which lies significantly below the universal curve (figure 17*b*). The two cross-stream spectra are statistically identical: figure 18(*b*) shows a clear tendency for spectral estimates to fall below the universal curve at low wavenumbers (although individual points may not be significantly different from the universal curve, the ensemble average of all 4 records certainly is). These features of the evolution of the energy-containing scales, namely maintenance of a $-\frac{5}{3}$ subrange in ϕ_{11} while $\phi_{22} = \phi_{33}$ falls below the universal curve at low wavenumbers, are even more clearly seen in the variance-preserving forms of figures 19(*a*) (ϕ_{11}) and (*b*) (ϕ_{22} and ϕ_{33}). These figures also contain the dissipation spectra; despite evidence of developing anisotropy

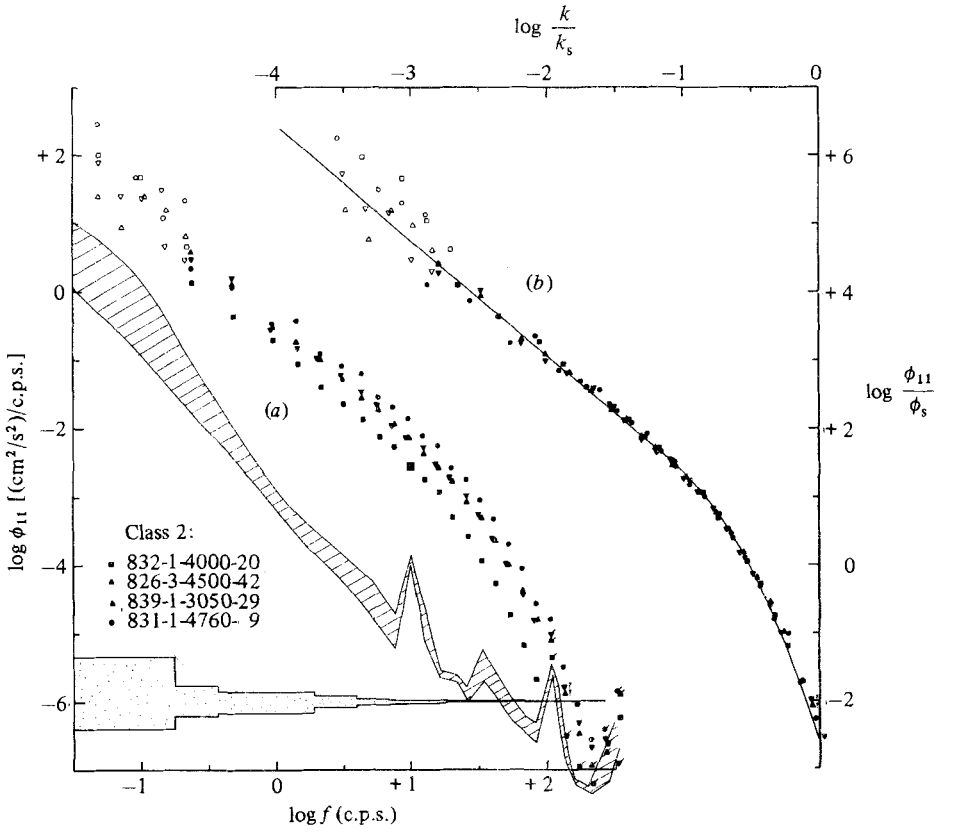

FIGURE 17. (*a*) Dimensional spectra ϕ_{11} as a function of frequency for Class 2 records: solid and open symbols are results from the heated-film and rotor triplet respectively. Lower signal levels than Class 1 records leads to rejection of some spectral estimates (flagged) at high frequencies. Statistical error bars are plotted for the record with the minimum number of degrees of freedom. (*b*) Kolmogoroff-scaled spectra. Scatter at low frequencies is attributed to submersible motions.

in the (energy-containing) low wavenumbers, each of the three component spectra joins its appropriate universal curve by wavenumbers which contribute significantly to the area under the curve.

Class-averaged spectral ratios are shown in figure 20: open (closed) triangles are ϕ_{22}/ϕ_{11} (ϕ_{33}/ϕ_{11}). The bandwidth in logarithm of non-dimensional wavenumber has been chosen to average $\sim$ 6–8 estimates (rather than the 4 estimates averaged to produce figure 11), avoiding 'holes' in the ratios due to rejection of vibration-contaminated estimates of ϕ_{22} or ϕ_{33} (at fixed frequencies). Error bars about the $\frac{4}{3}$ ratio calculated with the total number of degrees of freedom in each class: these are approximately equal for the three classes (2 (100), 3 (103) and 4 (109)) and the theoretical spread about $\frac{4}{3} = 1.33$ is $\sim$ (0.96, 1.85) at the lowest estimates seen in figure 20. Theoretical error bounds are harder to calculate at higher non-dimensional wavenumbers, because the spread in values of ϵ_1 among the records distributes the constant dimensional wavenumbers at which spectral estimates are calculated: instead we choose to use the standard deviations as a direct error estimate. To avoid confusion in figure 20, standard deviations are plotted only when the two cross-stream/streamwise ratios for a particular record *differ* by more than their standard deviations; otherwise, errors are equal to or greater than the difference between the

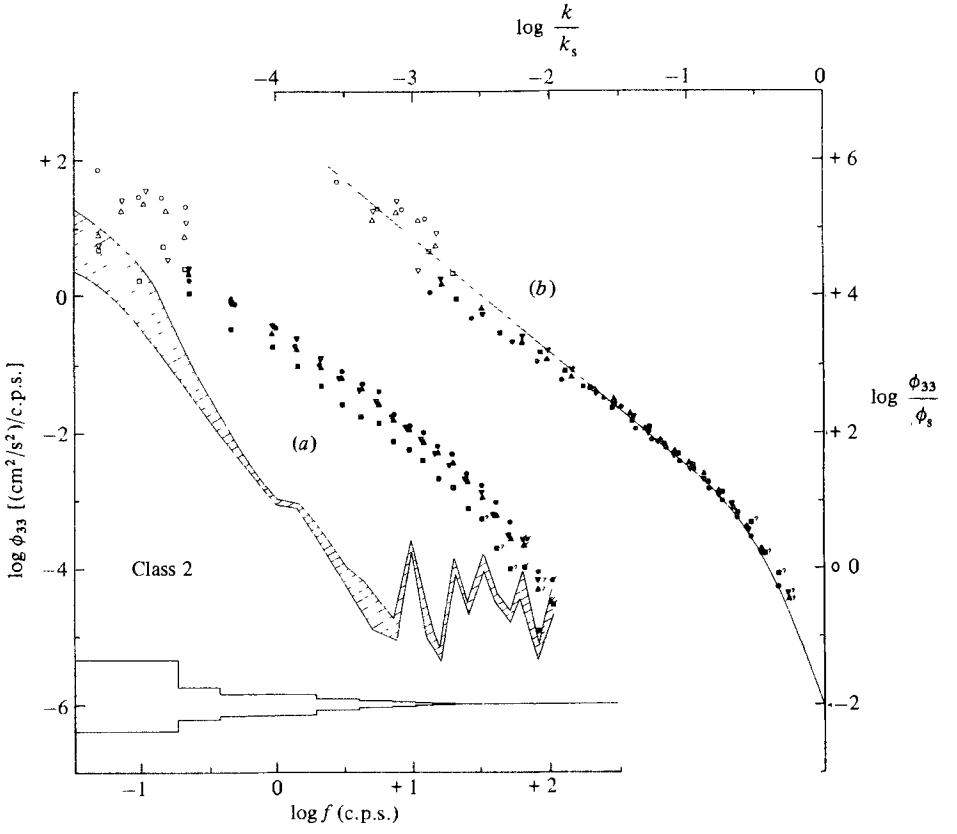

FIGURE 18. (*a*) Non-dimensional spectra ϕ_{33} as a function of frequency for Class 2 records: solid and open symbols are results from the w-component airfoil and the rotor triplet respectively. Lower signal levels than the Class 1 records lead to rejection of all spectral estimates at the combined 5th and 6th harmonic of the fundamental vibration peak and a few at higher frequencies. Rotor-derived estimates at low wavenumber may indicate a broad peak around a frequency of ~ 0.1 Hz, possibly associated with slight pitching motions induced by variations of current on the scale of the submersible. Below this, levels generally fall to the noise level, suggesting that the turbulent signal spectrum is considerably lower. (*b*) Kolmogoroff-scaled spectra: the ϕ_{22} spectra (not shown) are statistically identical.

two ratios. Throughout the range of Class 2 ratios, $\phi_{22}/\phi_{11} = \phi_{33}/\phi_{11}$ within their standard deviations.

Figure 20 demonstrates two features of the Class 2–4 ratio values. First, ratio values droop below $\frac{4}{3}$ at low wavenumbers; this is caused by the observed droop of the cross-stream component spectra below their inertial subrange, rather than by change in the streamwise component. Secondly, there is a strong tendency for ratio values to reach the expected isotropic curve by dissipation scales (note that 90 % of the area beneath the isotropic cross-stream dissipation curve lies above the wavenumber $k_2/k_s \approx \frac{1}{15}$ marked in figure 20). Thirdly, the point at which the isotropic ratio curve rises above $\frac{4}{3}$ roughly coincides with the beginning of the wavenumber range in which molecular viscosity acts directly on the velocity field. The tendency of the ratios to lie slightly above the universal curve at high wavenumber is similar to the Class 1 ratios and may be attributed to the same causes.

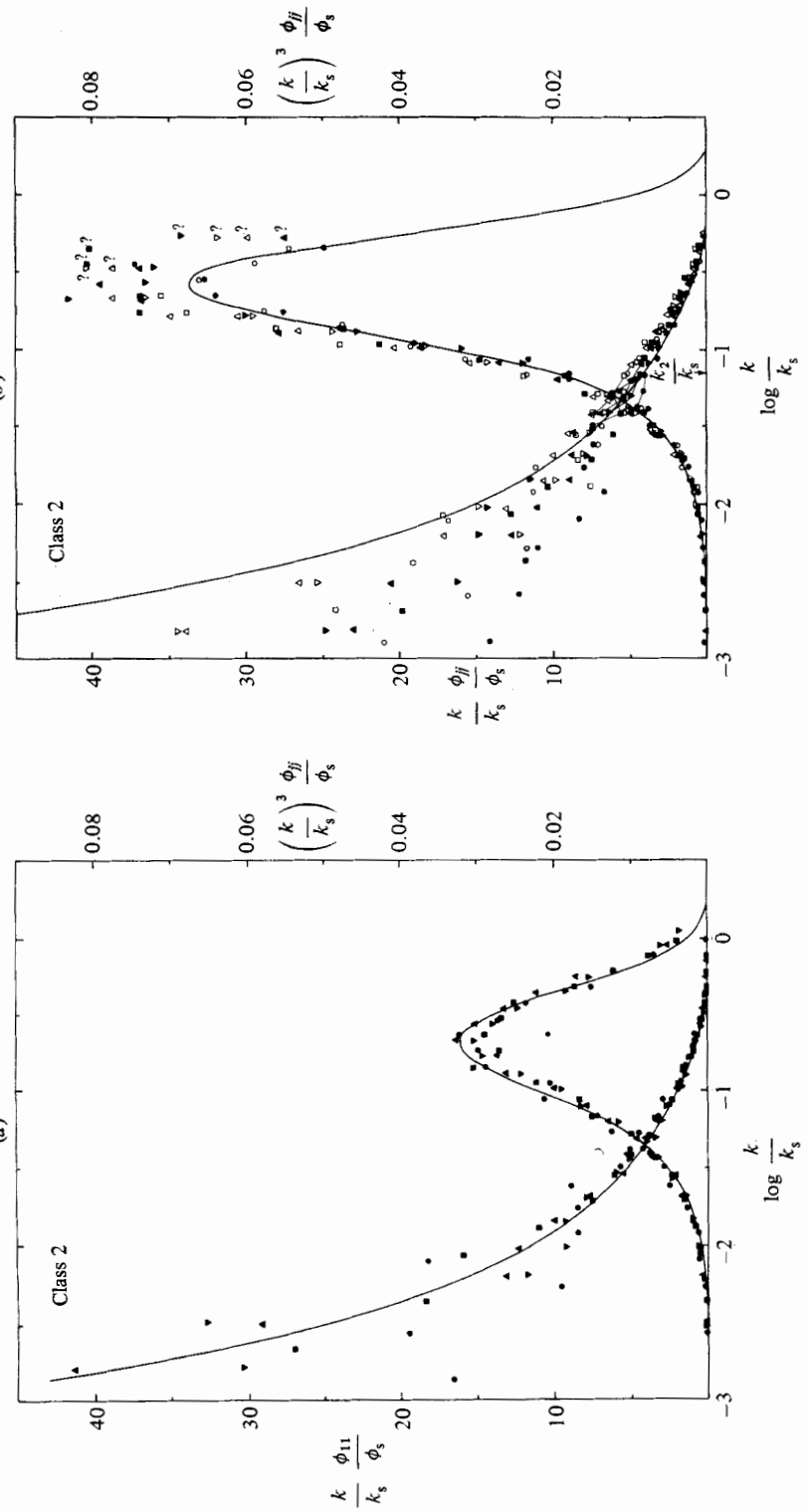

FIGURE 19. Variance-preserving energy and dissipation spectra for (*a*) streamwise and (*b*) v (open symbols) and w (closed symbols) cross-stream spectra for Class 2 records. Cross-stream components fall below their universal curve at low wavenumbers, but reach it by scales which contribute significantly to the dissipation spectrum (90 % of the area beneath the dissipation curve lies above the non-dimensional wavenumber k_2/k_s). Scatter about the peak is caused by increased influence of high-frequency vibration at the lower (dimensional) signal levels of this class.

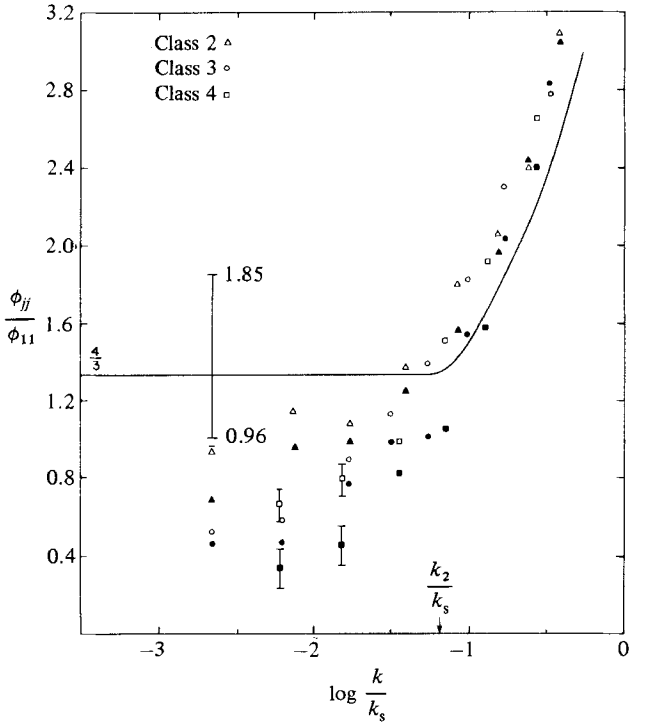

FIGURE 20. Class-averaged ratios of cross-stream/streamwise velocity components: open and closed symbols refer to horizontal ($j = 2$) and vertical ($j = 3$) cross-components respectively. For discussion of error bars see §5.1. Class 2 ratios fall significantly below the isotropic $\frac{4}{3}$ ratio at the lowest wavenumber, while Class 3 ratios are lower still. For all estimates shown without error bars, $\phi_{22}/\phi_{11} = \phi_{33}/\phi_{11}$ within the standard deviation of the estimates averaged. Only in the lowest two estimates of the Class 4 records (standard deviations shown) is there statistically significant evidence of preferential removal of energy from vertical rather than horizontal cross-component.

5.2. *Class* 3 *records*: $200 < I < 300$

Dimensional and non-dimensional plots of component spectra for Class 3 records are presented in figures 21 (ϕ_{11}) and 22 (ϕ_{33}): again ϕ_{22} is statistically identical with ϕ_{33}. Although the axial component spectrum still maintains an acceptable $-\frac{5}{3}$ subrange, values are beginning to fall slightly below the universal curve (most clearly seen in the variance preserving energy spectrum of figure 23*a*). The decrease is not statistically significant in Class 3 spectra: however, it proves significant when seen from the vantage point of Class 4 records in which, with further decrease in I, ϕ_{11} does fall significantly below the universal curve in what was inertial subrange. The cross-stream spectra, while still statistically indistinguishable, have by now developed a distinct -1 subrange connecting a steeper ($-\frac{5}{3}$?) slope at lower wavenumbers to the universal curve at higher wavenumbers. This behaviour is most clearly seen in the variance-preserving energy spectrum of figure 23(*b*), where the -1 subrange appears as a short but distinct plateau. Spectral ratios for this class (circles in figure 20) show a decrease from the Class 2 ratios at the lower wavenumbers, but the same strong tendency to climb steeply to the isotropic ratio curve once dissipation scales are reached.

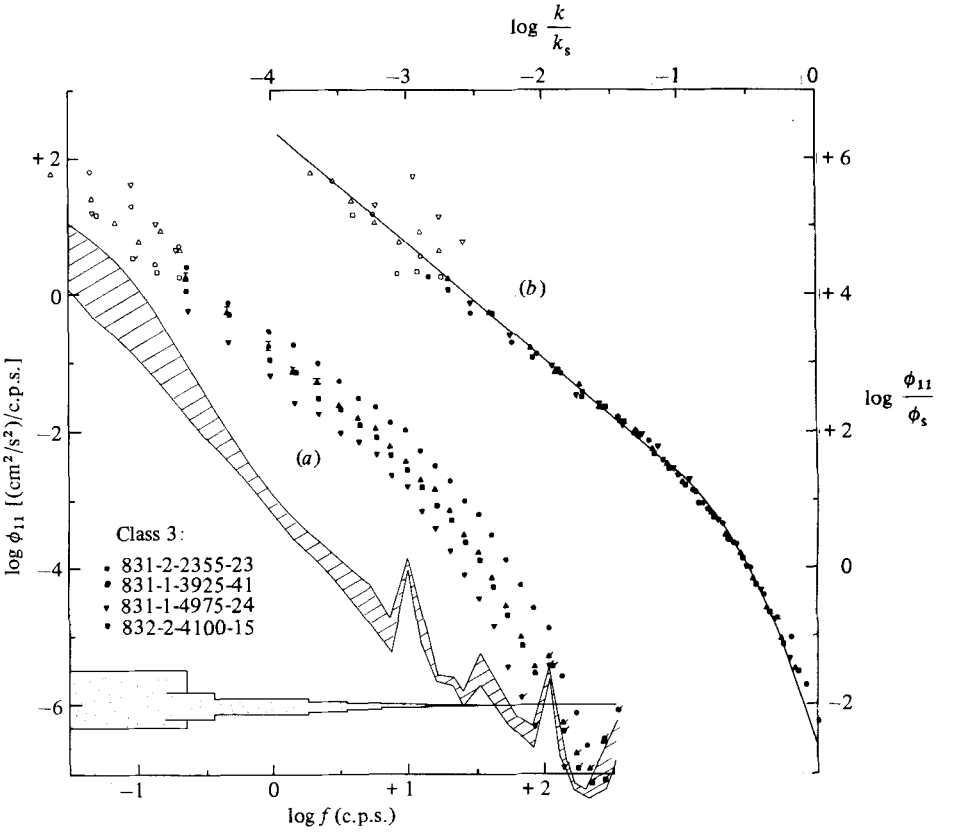

FIGURE 21. (*a*) Dimensional plots of ϕ_{11} as a function of frequency for Class 3 records: for further details see caption to figure 17(*a*). (*b*) Kolmogoroff-scaled spectra: the slight tendency for ϕ_{11} to fall below the universal curve in the inertial subrange is not statistically significant here, but will become so in the next class.

5.3. *Class 4 records*: $50 < I < 100$

The lowest values of I are associated with the lowest signal levels and consequently the highest rate of data rejection. At the low-wavenumber end of dimensional spectra shown in figures 24 (ϕ_{11}) and 25 (ϕ_{33}), all of the rotor-derived estimates and some estimates from the high-frequency sensors have been rejected. There is also substantial data rejection at high frequencies, particularly in the cross-stream spectra (fortunately, as ϵ decreases the peaks of the dissipation spectra shift to lower dimensional wavenumber (frequency) so loss of high frequencies is not as serious as it might seem). In figure 24(*b*) note the significant decrease of ϕ_{11} below the inertial subrange of the universal curve. Within the dissipation range, agreement between measurements and the universal curve is still reasonable, although there appears to be a tendency for the measurements to be shifted to slightly higher wavenumbers (figure 26*a*). This may be partly a result of our standard practice of using the last point significantly above noise level to terminate the calculation of ϵ_1. For the Class 4 records, this results in slightly underestimating ϵ_1 (by a maximum of $\sim 15\,\%$) and hence k_s (by a maximum of $\sim 4\,\%$) and leads to a shift which, although slight, is in the observed direction.

Cross-stream energy spectra again exhibit -1 subranges, clearly evident in the ϕ_{33} spectra shown in figures 25 and 26(*b*). Within the dissipation range, the cross-stream

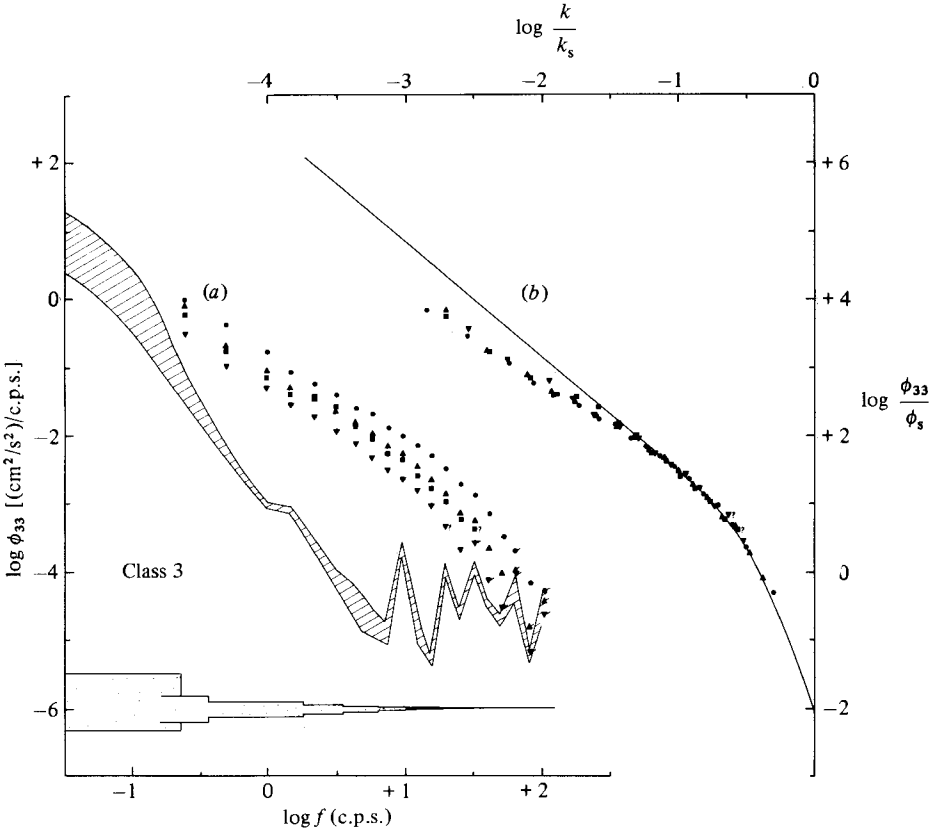

FIGURE 22. (*a*) Dimensional plots of ϕ_{33} as a function of frequency for Class 3 records. Low-frequency estimates from the rotor triplet are almost all at noise level and have been omitted: solid symbols are results from the w-component airfoil. Lower signal levels lead to increased rejection of high-frequency estimates; second and third harmonics of the fundamental vibration frequency are also starting to cause rejection or possible contamination (?) of the lower energy records. (*b*) Kolmogoroff-scaled spectra: the ϕ_{22} spectra (not shown) are statistically identical.

spectra roughly approximate the universal curve, although there is a tendency for measured values to lie slightly below the universal dissipation spectrum in the steep rise to its peak (figure 26(*b*), especially record 838-1-1075 (squares)).

Class-averaged cross-spectral ratios (squares in figure 20) are similar in magnitude to those of the Class 3 spectra, but there is now a significant difference between horizontal and vertical cross-components at the two lowest spectral estimates. This may, finally, be evidence of preferential loss of energy by the vertical component of the decaying turbulence. This evidence appears first at low wavenumbers: by dissipation scales, the ratios reach the same isotropic ratio curve as the other classes.

6. Buoyancy scaling

As shown in §§4 and 5, Kolmogoroff scaling is quite successful in collapsing all measured spectra to universal forms in the dissipation range of wavenumbers: one example from each class is shown in figure 27(*a*). For the energy-containing low-wavenumber range the value of the buoyancy scaling mentioned in §1 can be

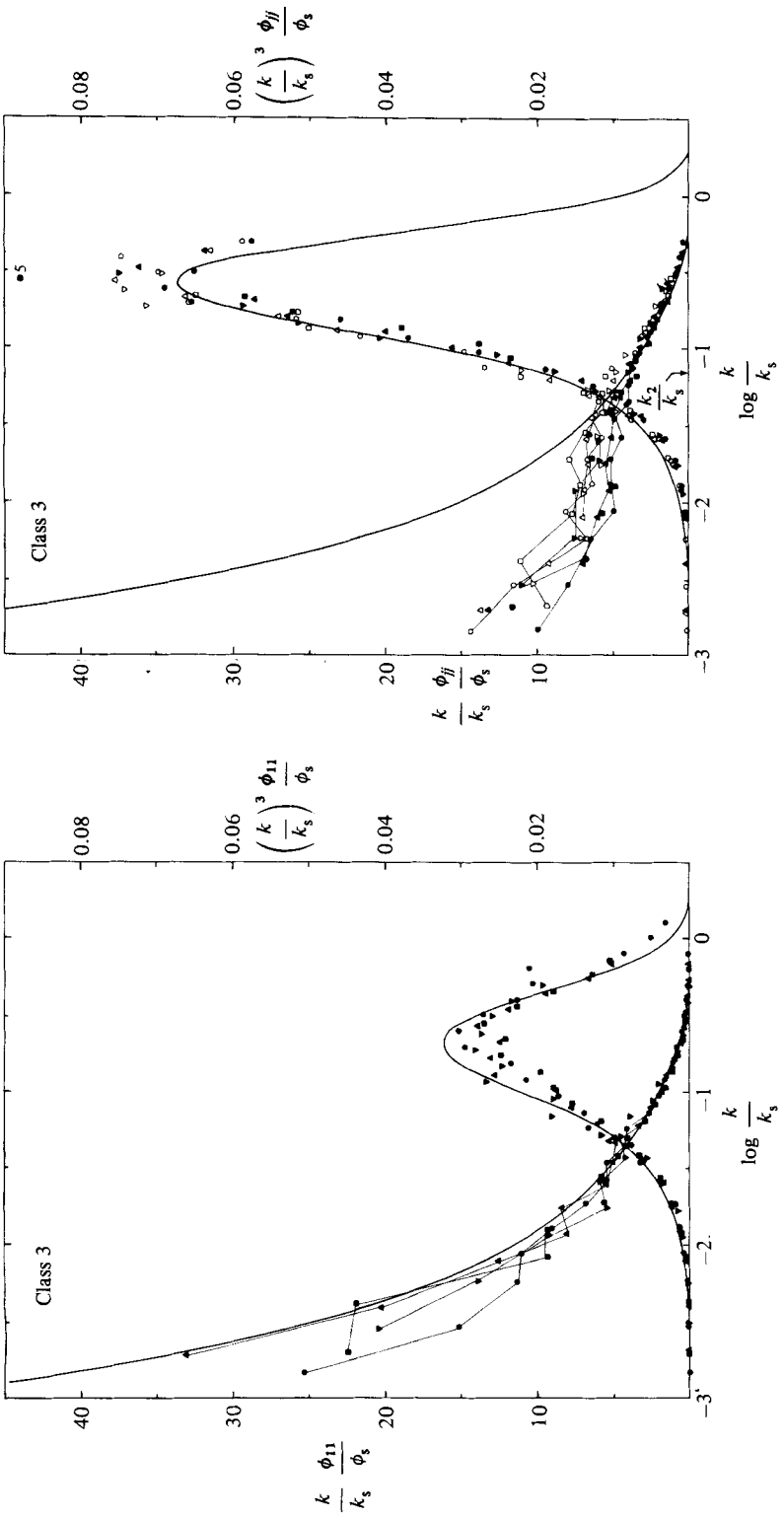

FIGURE 23. (*a*) Variance-preserving energy and dissipation spectra for the stream-wise velocity component records of Class 3: measurements generally follow the isotropic curves, although a tendency for points to fall below the energy curve at the lowest wavenumbers is discernible. (*b*) Variance-preserving energy and dissipation spectra for v (open symbols) and w (closed symbols) cross-component spectra of Class 3. Energy spectral values at low wavenumbers are dramatically below the universal curve. In this representation the plateau in the energy spectra between $k/k_s \approx 10^{-2.2}$ and $10^{-1.5}$ corresponds to a -1 subrange in the velocity spectra. Measured spectra agree well with the universal curve through the dissipation range.

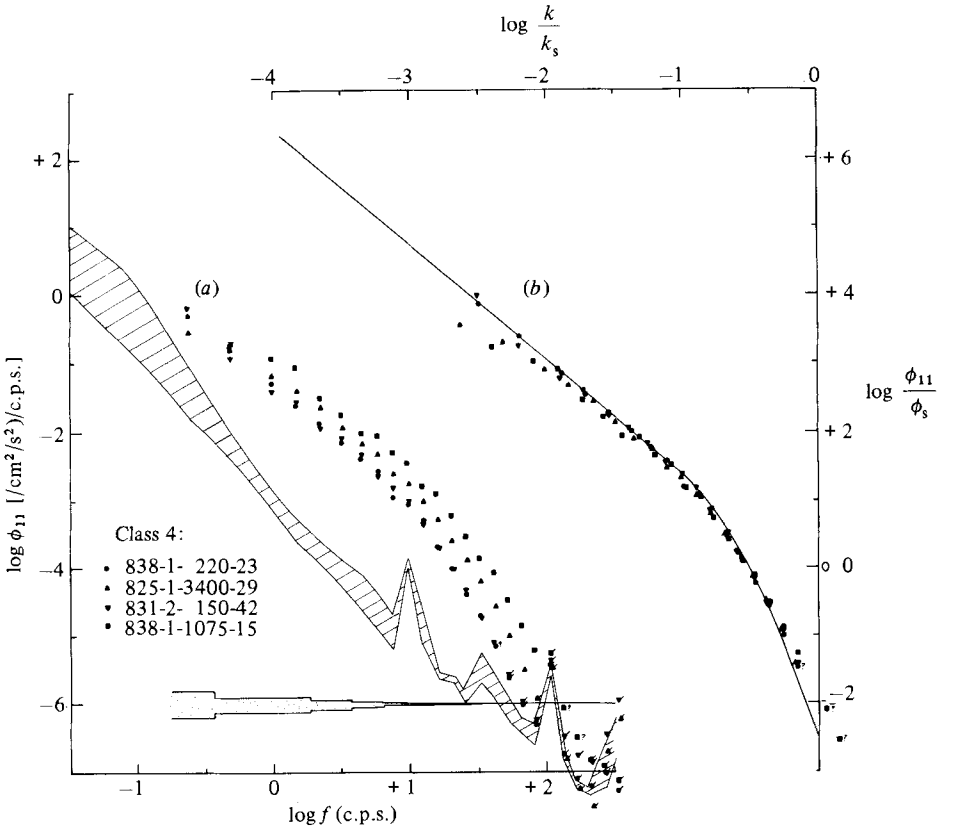

FIGURE 24. (*a*) Dimensional plots of ϕ_{11} as a function of frequency for Class 4 records. Low-frequency estimates from the rotor triplet have fallen to the noise levels and are not plotted: solid symbols are results from the heated-film. Flagged estimates are rejected on the basis of noise contamination. (*b*) Kolmogoroff-scaled spectra collapse to the universal curve at high wavenumbers, but lie progressively below it at lower wavenumbers.

seen in figure 27(*b*), where scaling by k_b and $\phi_b \equiv u_b^2/k_b$ produces satisfactory low-wavenumber normalization. In particular, note that the levels of the vertical velocity spectra are successfully collapsed to a 'universal' level over the k^{-1} range: moreover the junction of this range with the $k^{-\frac{5}{3}}$ range for ϕ_{33} is collapsed to $k \approx 10\,k_b$.

The success of this normalization is perhaps more readily appreciated in linear (variance-preserving) plots. In the scaled streamwise component spectra of figure 28(*a*) note the presence of a well-defined peak, of magnitude $k\phi/k_b\phi_b \approx 0.45$–$0.50$ near $k = k_b$ in Class 2 (▲) and Class 4 (■) records. (Conclusive resolution of such a peak is marginal in the records of Class 1 because record lengths are only $\sim l_b$ long, and in Class 3 because measured spectral levels near $k \sim k_b$ are generally close to the low-wavenumber noise level due to vehicle motion.) The vertieal cross-component spectra (figure 28*b*) show a distinct development during decay. The Class 1 record has a $k^{-\frac{2}{3}}$ inertial range behaviour in this representation. As the turbulence decays, a shelf starts to develop (Class 2 (▲)), reaching from $k \sim 10\,k_b$ down to progressively lower wavenumbers (Class 3 (▼) and 4 (■)) at a nearly constant level $k\phi/k_b\phi_b \approx 0.15$–$0.20$. Below the low-wavenumber end of the shelf, levels again rise more steeply in those Class 2 or 3 records which are above noise in this range. In some Class 4 records there is the suggestion that the extension of the shelf (corresponding to the k^{-1} range

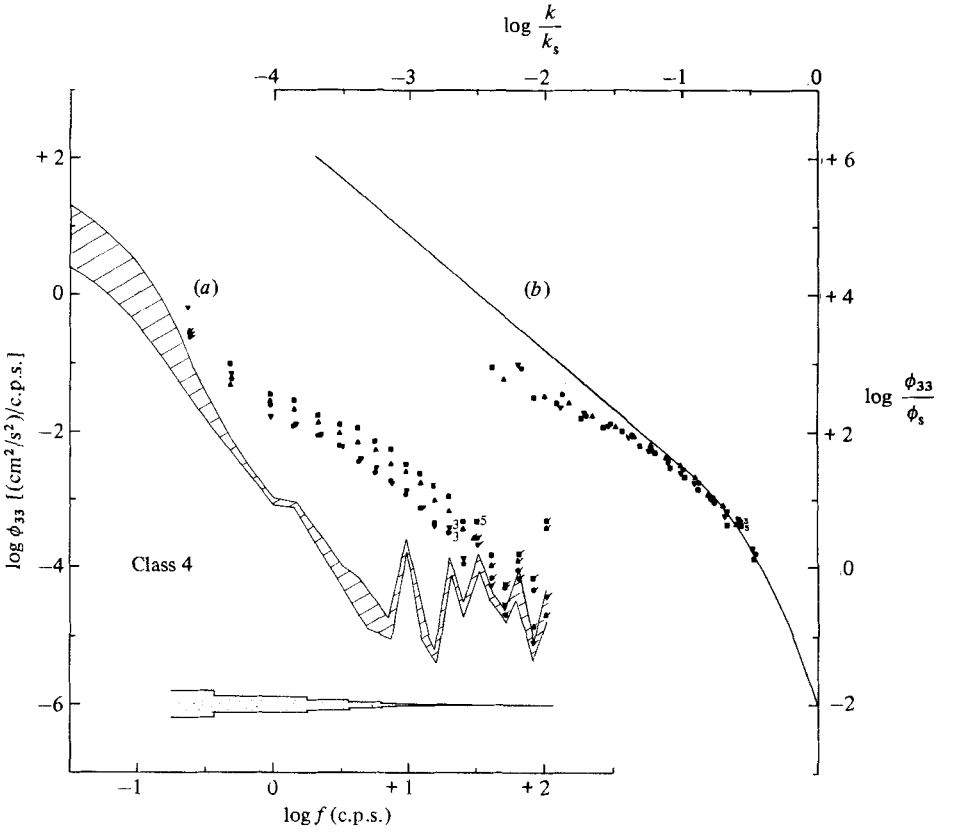

FIGURE 25. (*a*) Dimensional plots of ϕ_{33} as a function of frequency for Class 4 records. (*b*) Kolmogoroff-scaled spectra exhibit a clear -1 range, approaching the universal curve by dissipation scales. The ϕ_{22} spectra are statistically identical at all save the two lowest wavenumber estimates, where $\phi_{22} > \phi_{33}$.

of the ϕ_{33} spectrum) does not proceed to indefinitely small wavenumbers, but only to $k \sim k_b$. Buoyant-turbulence scaling does not of course collapse the high-wavenumber ranges ($k \gtrsim 10\ k_b$) of figure 27(*b*), where Kolmogoroff scaling is successful, but these ranges make relatively minor contributions to the velocity variances.

As discussed by Gargett (1982) and obvious in the data presented here, vehicle motion makes it difficult to determine the energy-containing scales of turbulence from submersible measurements. However, there is considerable interest in the magnitudes of the velocity component variances, as a measure of the degree of anisotropy that develops in the turbulent kinetic energy as a result of the observed degree of departure of spectra from isotropic shapes. Encouraged by evidence of a spectral peak in ϕ_{11}/ϕ_b near $k \sim k_b$, we have estimated velocity-component variances from our measurements under the assumption that the energy-containing bandwith is $\frac{1}{2}k_b \lesssim k \lesssim 10\ k_b$; i.e.

$$u_i^2 \equiv \int_{\frac{1}{2}k_b}^{10\,k_b} \phi_{ii}(k)\,\mathrm{d}k.$$

All Class 4 records are resolved through $k \leqslant \frac{1}{2}k_b$. A few Class 3 records and most Class 2 records are resolved to only $k \sim k_b$, and these have been extrapolated to $\frac{1}{2}k_b$ using a $k^{-\frac{5}{3}}$ dependence for all three components (note that this assumes a $k^{-\frac{5}{3}}$ dependence

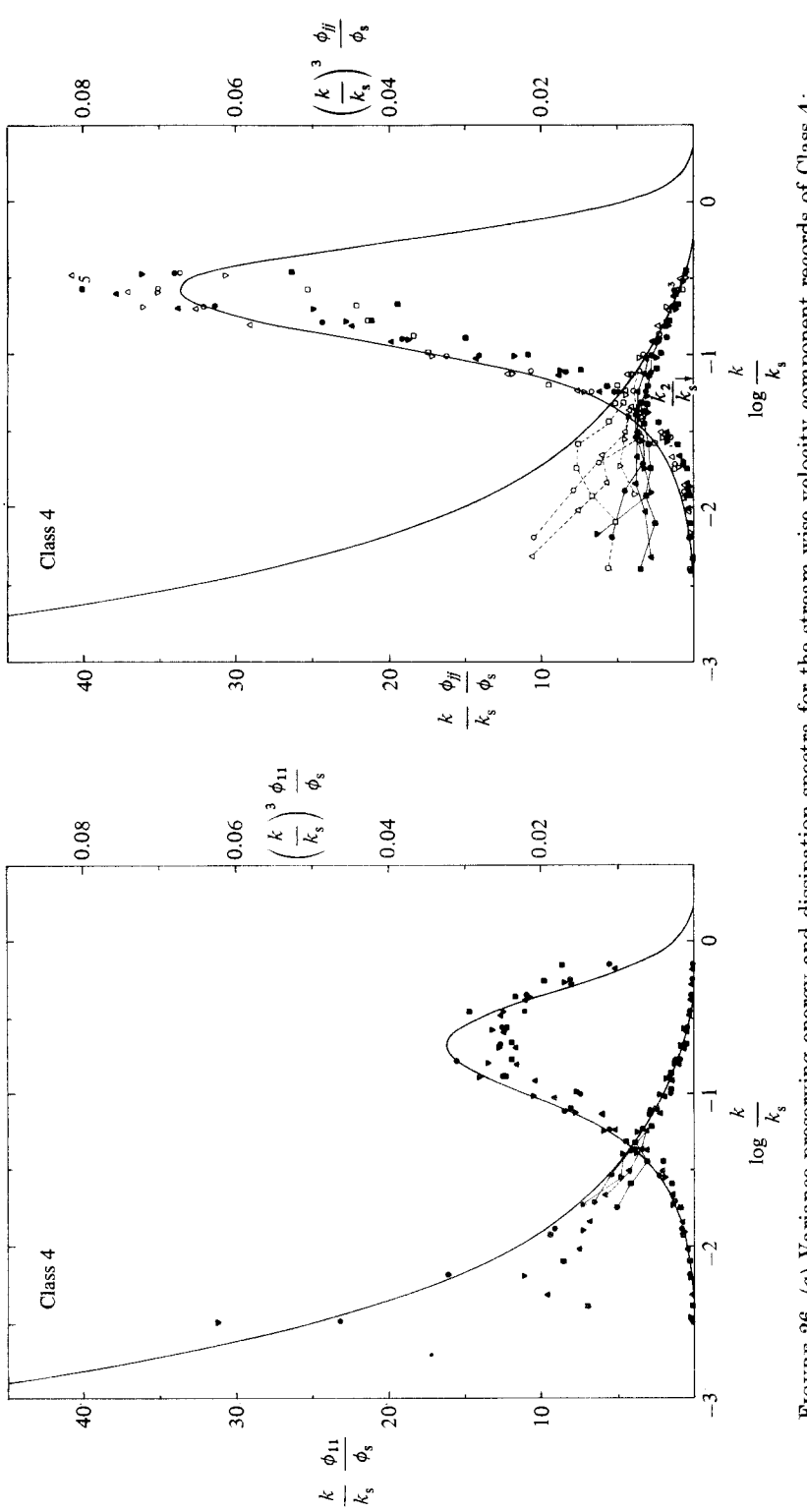

FIGURE 26. (*a*) Variance-preserving energy and dissipation spectra for the stream-wise velocity component records of Class 4: decrease of measured estimates below the universal curve has extended to higher non-dimensional wavenumbers than the Class 3 records. Values still reasonably approximate the universal curve at dissipation scales. (*b*) Variance-preserving energy and dissipation spectra for v (open symbols) and w (closed symbols) cross-component spectra of Class 4. The ϕ_{33} energy spectrum continues to show a flat region corresponding to the -1 region in the log/log plot of figure 25(*b*): this plateau is less evident in ϕ_{22}, possibly because of its higher noise level. The measured spectra, particularly ϕ_{33}, join the universal curve at higher wavenumber than the Class 3 records and there is a distinct tendency for the values to lie slightly below the universal dissipation curve in its steeply rising portion.

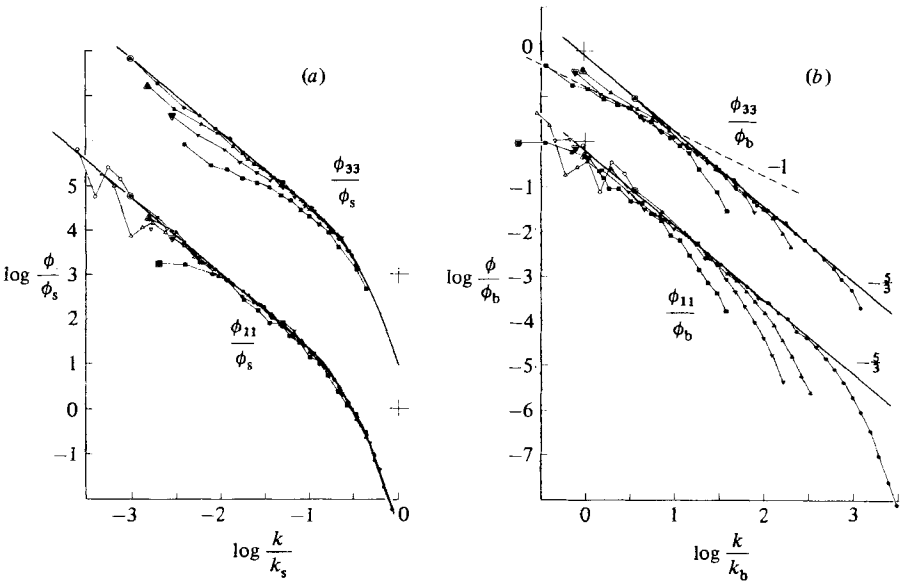

FIGURE 27. (*a*) Typical streamwise (ϕ_{11}) and vertical (ϕ_{33}) velocity component spectra from each of the four classes discussed in §§4 and 5, scaled by Kolmogoroff variables k_s and ϕ_s.

Class 1 (825-2-2725); Class 2 (839-1-3050);
Class 3 (832-1-4975); Class 4 (838-1-1075).

Open symbols on the plot of ϕ_{11}/ϕ_s are estimates derived from the low-frequency channel of the heated-film axial-velocity sensor (§3.1): only values greater than 3 times the low-frequency vehicle induced noise level are used. Crosses mark the origins for each plot. Kolmogoroff scaling successfully collapses the observed spectra at the high wavenumbers typical of dissipation scales, but does not describe the lower wavenumber range in which the energy resides. (*b*) The same spectra are shown here scaled by the buoyant-turbulent variables k_b and ϕ_b. This scaling is reasonably successful in collapsing the low-wavenumber end of the measured spectra, particularly the -1 region of the ϕ_{33} spectra.

of the cross-component spectra below the low-wavenumber end of the k^{-1} range, although the exact spectral shape in this range is not well determined).

Table 3 indicates that $\overline{u_1^2} \approx 1.2\,u_b^2$ throughout the decay process. In Class 2, $\overline{u_1^2} \sim \overline{u_2^2} \sim \overline{u_3^2}$ within the (large) scatter of the estimates, suggesting that the decay process had not substantially altered the equipartition of kinetic energy among components, although it had already begun to alter spectral shapes. By Class 3, $\overline{u_2^2} \sim \overline{u_3^2} \approx 0.7\,u_b^2 < \overline{u_1^2}$: energies of the cross-components have both become significantly less than that of the axial component. Class 4 is characterized by $\overline{u_2^2} \sim \overline{u_1^2} > \overline{u_3^2}$, a situation that may be suggestive of change towards a state of 'two dimensional' turbulence, in which motions remain chaotic and highly structured in the horizontal (isopycnal) plane, while vertical motions disappear.

Class 1 records are not included in table 3 because they are generally resolved only down to $k \sim (2\text{–}3)\,k_b$, short of the energy-containing peak. If extrapolated to $k \sim \frac{1}{2}k_b$ using a $k^{-\frac{5}{3}}$ dependence as may be appropriate for these records, the scaled variances are $\overline{u_1^2} \sim \overline{u_2^2} \sim \overline{u_3^2} \sim (2\text{–}3)\,u_b^2$.

7. Discussions and conclusions

The turbulent flow fields in Knight Inlet have many aspects reminiscent of laboratory flows used to study the decay of grid-generated turbulence in the presence of stable stratification (e.g. Dickey & Mellor 1980; Lange 1982; Stillinger, Helland

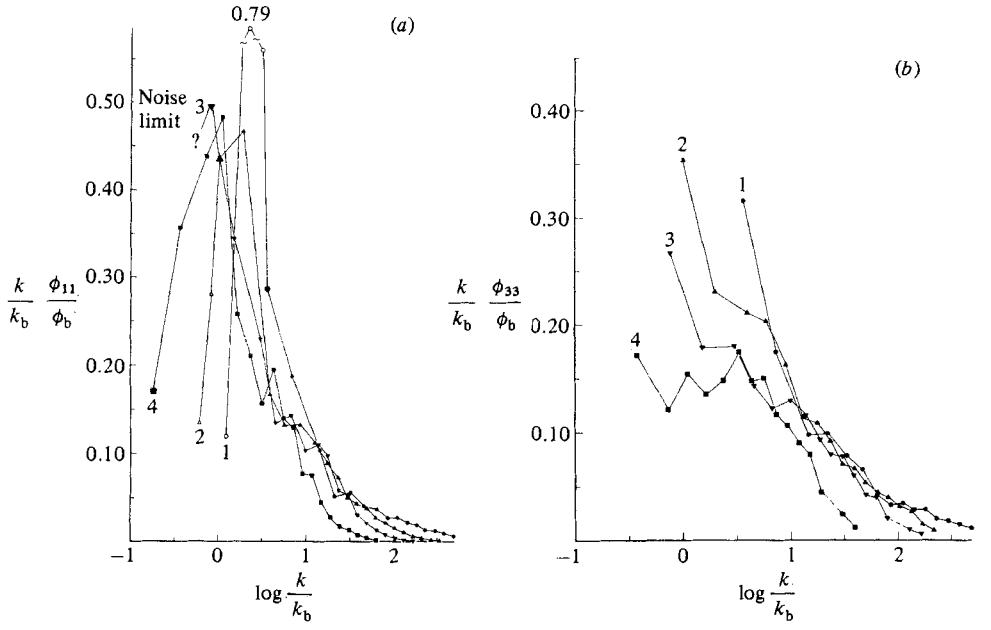

FIGURE 28. Variance-preserving plots of the buoyancy-scaled spectra of figure 27(*b*). (*a*) Signal strengths of the Class 1, 2, and 4 records are such that a spectral peak in ϕ_{11}/ϕ_b in the neighbourhood of $k \sim k_b$ is clearly delineated before the signal falls near the low-wavenumber noise level. (*b*) As decay proceeds (Class 1 → Class 4), this representation of the vertical spectrum develops a plateau which extends to wavenumbers progressively below $k \sim 10\,k_b$.

Class	$\overline{(u_1)^2}/u_b^2$	$\overline{(u_2)^2}/u_b^2$	$\overline{(u_3)^3}/u_b^2$
2	1.7	1.5	1.2
	0.85	0.90	0.60
	1.5	1.7	1.3
	1.3	1.0	0.70
	1.3 ± 0.35	1.3 ± 0.38	0.95 ± 0.35
3	1.4	0.8	0.8
	0.80	0.7	0.5
	1.1	—	0.5
	1.3	0.8	0.6
	1.2 ± 0.26	0.77 ± 0.06	0.60 ± 0.14
4	1.5	1.3	0.70
	1.1	1.2	0.65
	1.0	1.1	0.50
	1.2	0.95	0.65
	1.2 ± 0.22	1.1 ± 0.15	0.63 ± 0.09

TABLE 3. Velocity component variances expressed as a multiple of $u_b^2 \equiv \epsilon/N$.

& Van Atta 1983, henceforth referred to as SHV). The channel (fjord) and the mean (tidal) flow are basically two-dimensional, as are most laboratory facilities. The turbulent fields are quasi-steady with respect to the front of the internal wavetrain on flood tide, or the point of boundary-layer separation at the ridge on ebb tide: either may be identified with the turbulence-generating grid of the laboratory. With respect

to distance downstream of the generation region ('grid'), the turbulence in both systems decays under the influence of the background stratification. A major difference between inlet and laboratory is the Reynolds number characteristic of each. Using mean-flow (or tow) speed U and grid mesh size M, the maximum mesh Reynolds numbers $Re_M = UM/\nu$ for the experiments referenced above were 48260 (Dickey & Mellor 1980), 48000 (Lange 1982) and 4700 (SHV). In Knight Inlet the wavetrain ('grid') moves at $U \sim 0.5$ m s^{-1}, while acoustic records indicate a vertical scale of order $L \sim 10$ m in the leading wave: an equivalent mesh Reynolds number appears to be of order 4×10^6. During decay *both* the velocity and the lengthscale may decrease by a factor of 10 before the Reynolds number decreases to a value comparable to the largest values achieved in the laboratory. (An equivalent mesh Reynolds number for the separated boundary-layer flow is probably comparable to that for the wavetrain: although the mean tidal velocity over the sill is less than 0.5 m s^{-1}, the echo-sounder records indicate that the vertical scale of the initial instability is larger than 10 m.)

Large macroscopic Reynolds number implies that energy-containing scales are much larger than dissipation scales, a necessary condition for existence of an inertial subrange and its consequences in spectral slopes and ratios. The most intense turbulence observed in Knight Inlet (our Class 1 records) exhibit $-\frac{5}{3}$ inertial subranges in all three velocity-component spectra and nearly two decades of the expected isotropic $\frac{4}{3}$ ratio of cross-stream/streamwise component spectra. Verification of universal spectral shapes under Kolmogoroff scaling is enhanced by the fact that the heated film completely resolves the streamwise velocity dissipation spectrum, since an (isotropic) value of ϵ is directly determined and cannot be treated as an adjustable parameter in scaling to a 'universal' curve. These Class 1 records show no evidence of effects of stable density stratification over the wavenumber range measured: however as turbulence decays, the effects of stratification appear at the low wavenumber end of measured spectra. We find that the parameter $I \equiv k_s/k_b$ provides a reliable classification of the evolution of velocity spectral shapes under the combined effects of strong nonlinearity and buoyancy. As I decreases, spectral shapes and ratios evolve in predictable ways, as discussed in §5.

By examining both Kolmogoroff and buoyancy scalings, we have been able to establish a criterion for the existence of a 'true' inertial subrange, i.e. an inertial subrange supported by the isotropic $\frac{4}{3}$ ratio, in a particular stratified system. First we note that *all* observed spectra follow universal curves related by the isotropic relation (4) for wavenumbers $k \gtrsim 10\,k_b$. Thus the scaled wavenumber $10(k_b/k_s)$ is a *lower* boundary for possible $\frac{4}{3}$ range (in which cross-stream/streamwise component spectral ratios equal $\frac{4}{3}$), since this requires (at least) local isotropy. An *upper* boundary is the approximate scaled wavenumber $k_1/k_s \approx 0.1$ at which ϕ_{11} begins to roll off as dissipation becomes important (note that an isotropic ϕ_{11} spectrum departs from $k^{-\frac{5}{3}}$ behaviour before (i.e. at a lower wavenumber than) related cross-component spectra ϕ_{22} or ϕ_{33} (cf. figure 11*a*)). Thus the scaled wavenumber range over which spectral ratio values may be expected to achieve the value of $\frac{4}{3}$ is given by:

$$10\frac{k_b}{k_s} \gtrsim \frac{k}{k_s} \gtrsim \frac{1}{10}. \tag{14}$$

As an empirical result, (14) should be applied only to turbulent flows similar to those for which it is derived, i.e. those in which the energy-containing eddies scale with the buoyant-turbulence parameters u_b and l_b. It may not be relevant, for example, to the case of the near-surface region of a stratified boundary layer, where

surface friction velocity u_* is an additional velocity scale and distance z to the boundary is an additional lengthscale.

As the turbulence decays downstream of the generation region, ϵ decreases and the wavenumbers $k_b \propto \epsilon^{-\frac{1}{2}}$ and $k_s \propto \epsilon^{\frac{1}{4}}$ steadily approach one another, so that I steadily decreases. We have verified the assumption of dissipation-scale isotropy over the range of I-values spanned by the present observations, from $I \sim 3000$ for Class 1 records through $I \sim 50$ for the weakest Class 4 records. While the latter value may not quite be a lower bound, the Class 4 dissipation spectra begin to show slight but systematic deviations from expected isotropic curves. Thus the value of

$$L_L = \left(\frac{\epsilon_L}{\nu N^2}\right)^{\frac{3}{4}} = 50$$

has been used to evaluate a conservative lower limit $\epsilon_L = 50^{\frac{4}{3}}\nu N^2 \sim 200\nu N^2$ for the value of ϵ that may be estimated by measurement of a single component of the dissipation tensor and consequent assumption of dissipation-scale isotropy. We note that this value is larger than the value of $I_t \approx 11(\epsilon_t/\nu N^2 = 24.5)$ that SHV report as characteristic of turbulence at a point of transition to a 'saturated internal wave field'. Although SHV do not report a check of dissipation-scale isotropy for their stratified measurements, the result $I_t < I_L$ seems intuitively reasonable, since the process of obtaining ϵ from one component of the dissipation tensor must become a progressively worse approximation as I decreases further from the value I_L at which deviations for isotropy first begin to appear.

For the ocean, we may choose N-values of 1.2×10^{-2} rad s^{-1} (7 c.p.h.), 5.2×10^{-3} rad s^{-1} (3 c.p.h.) and 1.7×10^{3} rad s^{-1} (1 c.p.h.) as representative respectively of the seasonal thermocline (ST), the main thermocline (MT) and the deep ocean (D): then the above formula suggests that we may have full confidence in single-component determination of ϵ for values greater than or equal to respectively 7×10^{-8} m^2 s^{-3} (ST), 1×10^{-8} m^2 s^{-3} (MT) and 1×10^{-9} m^2 s^{-1} (D). A survey of available single-component estimates of ϵ in the stratified interior of the ocean (Gargett & Osborn 1981; Lueck, Crawford & Osborn 1983) reveals that the values that dominate an average over any depth interval lie comfortably above ϵ_L calculated with the average N over the interval. Thus is appears that reported oceanic values of ϵ are substantially correct, regardless of the degree of anisotropy which may occur at wavenumbers below those of the dissipation range. The character of the velocity field at these low wavenumbers is itself of general interest. Given the characteristics of the Class 1 records, we have no hesitation in calling these motions turbulent. As decay proceeds (Class 2 $\rightarrow$ 4), however, spectral shapes change (at the low-wavenumber end) and vertical kinetic energy clearly becomes somewhat depleted relative to horizontal kinetic energy. In these cases we ask whether perhaps the fields have decayed to the point where they still support an enhanced rate of kinetic energy dissipation, but have lost one of the important characteristics of turbulence, namely the ability to mix, i.e. to support a vertical mass flux $\overline{\rho' w'} > 0$. Since we did not measure $\overline{\rho' w'}$ we would have no answer to this question were it not for the timely observations of SHV, who made direct measurements of vertical mass flux and found that $\overline{\rho' w'}$ fell rather abruptly to zero at $I = 11$. Since even the weakest Class 4 records have substantially larger I-values, we conclude that all the turbulence discussed in this paper is still effecting vertical mass flux and should not be classified as a 'saturated internal-wave field'.

A final point of interest is the magnitude of the dominant vertical overturning length l_0: that is, while the buoyancy-scaled data suggest that $l_0 = C_0 l_b$ is indeed an

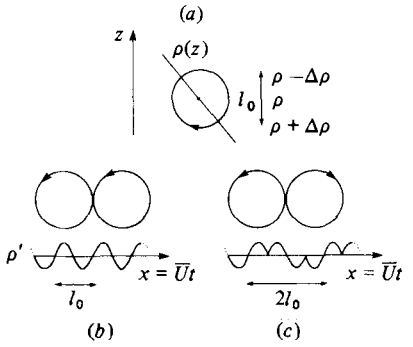

FIGURE 29. (*a*) Solid-body-rotation model of the large eddies of a turbulent field (after Stillinger *et al.* 1983). An eddy of size l_0, overturning in (stable) stratification $\rho(z)$, is associated with fluctuating density magnitude $\Delta\rho = l_0\rho_z$. (*b*) Schematic representation of the fluctuating density ρ' observed by a sensor moving at mean speed $\bar{U}$ through a field of corotating eddies. (*c*) Similar schematic for a field of counter-rotating eddies.

appropriate lengthscale, we would like to know the value of the order-one constant C_0. We first note that a lower bound on l_0 can be determined from the observation that all observed spectra reach isotropically related universal curves by $l \approx 0.1\, l_b$ ($k \approx 10\, k_b$). If the velocity field is to achieve isotropy at lengthscale l by cascade of energy from larger scales, the value $0.1\, l_b$ is clearly a generous lower bound on l_0. Moreover, it appears likely that l_b is an upper bound on l_0. Values of l_b average $\sim$ 12 m for Class 1 records, $\sim$ 5 m for Class 2 records, and $\sim$ 2 m for Class 3 records (table 2), but records of difference temperature over 0.8 m show a large proportion of measurably unstable values only for the Class 1 records, suggesting that $l_0 < l_b$. Thus $0.1\, l_b < l_0 < l_b$ for the Knight Inlet measurements (note that the corresponding wavenumber range $k_b \leqslant k_0 \leqslant 10\, k_b$ is, reassuringly, within the wavenumber range observed to contain the vertical velocity variance in those (Class 4) records which are completely resolved).

To further narrow the range within which the overturning scale must lie, we consider further results from SHV, who introduced a solid-body-rotation model (see figure 29) for the process of turbulent entrainment of density across a local density gradient ρ_z and used it to define a length L_T which was assumed to be proportional (if not exactly equal) to l_0, the scale of the largest vertically overturning eddy. A density sensor fixed at point P in a space full of such circular eddies records a fluctuating density $\rho' = \Delta\rho \sin\omega t$, where $\omega = 2\pi\bar{U}/l_0$ is the apparent frequency (due to eddies of size l_0 advecting past point P at mean speed $\bar{U}$), and $2\Delta\rho = l_0\rho_z$. Measured values of fluctuating density $\overline{(\rho')^2} = \frac{1}{2}(\Delta\rho)^2$ can thus be used to calculate

$$l_0 = \frac{2\sqrt{2}(\overline{(\rho')^2})^{\frac{1}{2}}}{\rho_z}. \tag{15}$$

We note that this scale is a factor of $\sqrt{2}$ *larger* than the lengthscale L_T defined by SHV (who used $\overline{(\rho')^2} = (\Delta\rho)^2$), but appears to be more consistent with their solid-body-rotation model. Observationally, SHV found that within the buoyancy-influenced range of their observations,

$$\frac{L_T}{L_R} = 1.4, \quad \text{where} \quad L_R \equiv \left(\frac{\epsilon}{N^3}\right)^{\frac{1}{2}} = \frac{1}{k_b} = \frac{l_b}{2\pi}.$$

Thus in the context of the solid-body-rotation model of figure 29, the dominant overturning lengthscale is

$$l_0 = \sqrt{2}\, L_T = \frac{\sqrt{2}\,(1.4)}{2\pi} l_b \approx \tfrac{1}{3} l_b \approx 2L_R, \tag{16}$$

a value within the previously derived bounds.

As a final check on the above calculation, we have calculated the scale l_0 (equation (15)) for Class 4 records, using the values of r.m.s. $T \equiv T'$ from table 1 and $\Delta T/\Delta z$ from table 2 and assuming $\rho' \propto T'$. This calculation is an acceptable approximation because temperature records associated with Class 4 velocity records have relatively little variance below the effective 0.5 Hz high-pass filter used to calculate r.m.s. T for the purposes of table 1: it is *not* appropriate for the other classes. The four Class 4 records yield $l_0 = (1.1 \pm 0.4)\,(\frac{1}{3} l_b)$, tending to support (16) above. However, since the value of $\overline{(T')^2}$ is quite sensitive to the low-wavenumber portion of the turbulent temperature spectrum, this result should be treated with caution at present: a detailed discussion of the associated temperature records from Knight Inlet is in preparation.

The observed vertical velocity spectra do not exhibit a clear peak at the wavenumber $k_0 = 2\pi/l_0 \approx 3\,k_b$ (or any other), presumably because the *Pisces* measurement path is horizontal and there is no buoyancy-related limit on the horizontal lengthscale of w, as there is on its vertical lengthscale. It remains to explain the peak that *is* observed in the spectrum of streamwise velocity, i.e. the velocity component in the (horizontal) direction of measurement. This peak, at a wavenumber $k_h \sim (1\text{–}2)\,k_b$, appears to be slightly lower than the wavenumber $k_0 \sim 3\,k_b$ associated with the above estimate of l_0. This separation between k_h and k_0 may prove an artifact, due to error in calculating k_b or some additional order-one constant involved in identification of 'the' vertical overturning scale with the scale l_0 derived from a simplistic model (see following). Note, however, that continuity requires that turbulence that decays preferentially in the vertical velocity component *must develop two lengthscales* during decay. Let u and w be typical magnitudes of horizontal ($u_1 \sim u_2 \sim u$) and vertical velocity components, l_h be a typical lengthscale for u, and l_0 be a typical *vertical* lengthscale for w; then continuity requires that $u/l_h \sim w/l_0$. If $w < u$ then $l_h \sim (u/w)\,l_0 > l_0$, or $k_h \sim (w/u)\,k_0 < k_0$. During the decay of turbulence under stable density stratification, we find that typically $w \approx \sqrt{\frac{1}{2}}\,u$ (Classes 3 and 4; see table 4); thus we might expect

$$k_h \sim \sqrt{\tfrac{1}{2}}\,(3\,k_b) \sim 2\,k_b,$$

consistent with the observations.

Despite some degree of success in comparing the present observations with the model of SHV, it should be pointed out that mechanistic models of the large eddies of a turbulent field may be misleading and should be applied with some caution, particularly when used to determine $O(1)$ constants. As an example, consider the question of whether the 'eddies' of figure 29(*a*) are corotating or counter-rotating (figures 29*b*, *c*). Again assuming sinusoidal eddies advected at constant speed, a measuring device would yield the fluctuating density records shown schematically below. Given long enough records, the spectrum of the record in figure 29(*b*) would peak at the wavenumber $k_0 = 2\pi/l_0$ corresponding to the 'eddy' scale l_0; the record of figure 29(*c*) would have spectral content down to $\frac{1}{2}k_0$, corresponding to the length $2l_0$, even though the size of each 'overturning' structure is only l_0.

In face of the above caveats, we still find it interesting to ask whether the value

$l_0 \sim \frac{1}{3} l_b$ that we obtain for a vertical overturning scale is consistent with oceanic observations of Gargett *et al.* (1981), who found that spectra of the vertical shear of horizontal velocity collapsed to a minimum near k_b when appropriately scaled with k_b and the *shear*-spectral density scale $(\phi_s)_b \equiv k_b u_b^2 = (\epsilon N)^{\frac{1}{2}}$. Imagining a vertical stack of identical 'eddies', each of vertical scale l_0, the horizontal velocity sensed by a vertically falling sensor will repeat identically over a distance l_0 if the eddies are corotating ($2l_0$ if they are counter-rotating). Thus $\partial u/\partial z$ due to the turbulent velocities will be zero at scale l_0 (or $2l_0$). Adding turbulent shears to a real background spectrum due to internal waves, we may thus expect a shear spectral minimum at a wavenumber between $(1.5\text{–}3)\,k_b$ for $l_0 \sim \frac{1}{3} l_b$, in reasonable agreement with the location of the broad shear spectral minimum observed by Gargett *et al.*

Finally, it should be remarked that the limitation of vertical scale is the most significant effect of stable stratification on turbulence. At least over the range of I-values observed in Knight Inlet, anisotropy of the turbulent motion is in some senses rather slight. The vertical velocity component is reduced only to about $\frac{7}{10}$ the magnitude of horizontal components (not to zero), and the energy-containing eddies appear to have horizontal lengthscales not more than twice their vertical scale.

Appendix. Determination of airfoil-probe response function

Airfoil probes have a limited wavenumber response owing to their physical size (diameter $d = 0.476$ cm). Siddon (1971) compared turbulence spectra from a cross-wire sensor and an airfoil probe operated in air, and found that the response of the airfoil began to fall at scales $\lambda \approx 4d$, which would be a scale of ~ 2 cm for the airfoils used on *Pisces*. Using a single-pole filter response with a cut-off wavelength of 2 cm, Oakey & Elliott (1982) found a reasonable fit between their measured shear spectra and a universal cross-stream shear spectrum derived from the axial component spectrum of Nasmyth (1970). Since their probes are of different manufacture and the degree of isotropy of their field measurements unknown, we have repeated this technique with the present data.

Specifically, we use the universal curve for $\phi_{11}(k)$ (generated by curve-fitting the four Class 1 records) in (4) to determine the universal curve $(\phi_{22})_u$ for $\phi_{22}(k)$. The curve in figure 30 shows the variance-preserving universal dissipation spectrum $(k/k_s)^2\,(\phi_{22}/\phi_s)_u$ as a function of k/k_s. This form provides maximum resolution in the area near and past the peak where measured cross-stream spectra fall below the universal curve: data from a Class 1 record are shown as circles ($j = 2$) and triangles ($j = 3$) in figure 30. The ratio of measured to expected values at each data point is an estimate of $R^2(k)$, the spectral response function of the airfoil probes at the dimensional wavenumber of the data point (which can be reconstructed from k/k_s and ϵ_1). Ideally, we would use only Class 1 records and would compute a separate response for each channel. However, since the roll-off region of the response curve is also that most affected by high-frequency vibrations, it was necessary to average a number of records together to achieve statistical confidence in the result. Thus we have treated both channels as identical (there is a consistent difference between ϕ_{22} and ϕ_{33} (evident in figure 30) at high wavenumbers, but it is not statistically significant), and have included portions of other records from Classes 2 and 3, selected by requiring that the spectral ratios ϕ_{jj}/ϕ_{11} achieve the isotropic ratio curve (figure 11*c*) before the airfoil signal rolls off due to spatial averaging. The response curve based on an average of 11 records is shown in figure 31. Heavy boxes refer to response determinations (by the rotation technique of Osborn & Crawford 1980) at 2.5 and

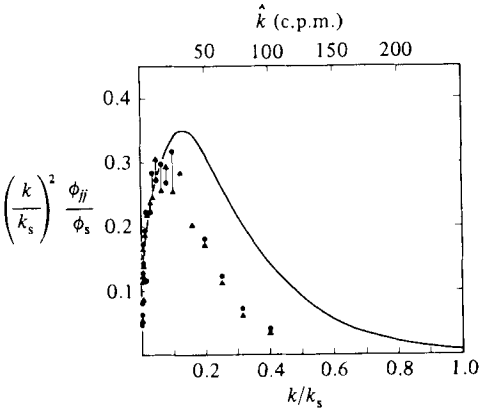

FIGURE 30. Variance-preserving plot of the universal cross-component dissipation spectrum (solid line), as derived from the axial-component (heated-film) spectrum under the assumption of isotropy. Symbols are the horizontal (circles) and vertical (triangles) cross-component spectra as measured by airfoil probes for a record that achieves the isotropic $\frac{4}{3}$ cross/axial component ratio for approximately a decade in wavenumber (figure 10) before rolling off at high wavenumber owing to finite probe size. Adjusting these measurements to the isotropic curve allows an estimate of the spatial response function of the airfoil probe.

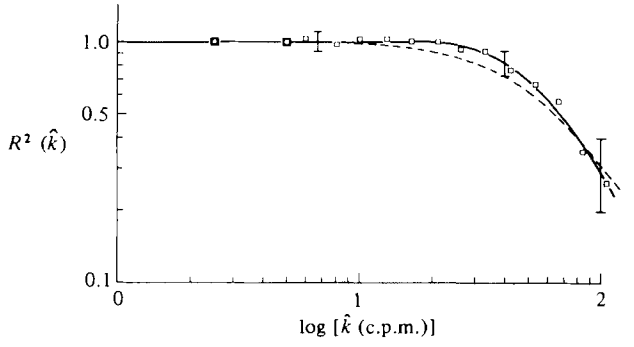

FIGURE 31. A polynomial fit (solid line) to averaged estimates (squares) of airfoil response as a function of wavenumber. The two airfoil channels are treated as identical for this purpose. Error bars (one standard deviation) rise toward high wavenumbers where vibrational contamination increasingly affects spectral estimates, decreasing the number of sample points. Also shown (dashed line) is the response function determined by Oakey & Elliott (1982) using the same technique. Differences between the two functions are of marginal significance in the range of 20 c.p.m. $> \hat{k} >$ 40 c.p.m.

5.0 Hz. Remaining points are from the technique described here; the error in $R^2(\hat{k})$ is $\sim \pm 0.1$, an error of 10% at low frequencies, rising to $\sim$ 40% by 100 c.p.m. An inverse polynomial fit to the response function (solid curve) gives the form $R^2(\hat{k}) = (1.033 - 8.836 \times 10^{-3}\,\hat{k} + 3.379 \times 10^{-4}\,\hat{k}^2)^{-1}$, which has been used to correct all the cross-stream spectra presented in this paper. Also shown (dashed curve in figure 31) is the single-pole filter response of Oakey & Elliott (1982). We do not know whether the difference between the two curves is due to increased accuracy of the present procedure or to physical differences between the probes.

REFERENCES

ANON. 1979 Oceanographic observations in Knight Inlet, B.C. Volume I: Salinity/Temperature Profiles. Part II: 1978. *Rep.* 79–12(2). *Inst. Ocean Sci., Patricia Bay, Sidney, B.C.*

BRITTER, R. E., HUNT, J. C. R. & MUMFORD, J. C. 1979 The distortion of turbulence by a circular cylinder. *J. Fluid Mech.* **92**, 269–301.

BUSCH, N. E. 1973 The surface boundary layer. *Boundary-Layer Met.* **4**, 213–240.

CHAMPAGNE, F. H. 1978 The fine-scale structure of the turbulent velocity field. *J. Fluid Mech.* **86**, 67–108.

CHAMPAGNE, F. H., HARRIS, V. G. & CORRSIN, S. 1970 Experiments on nearly homogeneous turbulent shear flow. *J. Fluid Mech.* **41**, 81–139.

DICKEY, T. D. & MELLOR, G. L. 1980 Decaying turbulence in neutral and stratified fluids. *J. Fluid Mech.* **99**, 23–31.

DILLON, T. M. & CALDWELL, D. R. 1980 The Batchelor spectrum and dissipation in the upper ocean. *J. Geophys. Res.* **85**, 1910–1916.

DOUGHERTY, J. P. 1961 The anisotropy of turbulence at the meteor level. *J. Atmos. Terr. Phys.* **21**, 210–213.

FARMER, D. M. & SMITH, J. D. 1977 Nonlinear internal waves in a fjord. In *Hydrodynamics of Estuaries and Fjords* (ed. J. Nihoul), pp. 465–493. Elsevier.

FARMER, D. M. & SMITH, J. D. 1980 Tidal interaction of stratified flow with a sill in Knight Inlet. *Deep-Sea Res.* **27A**, 239–254.

FREELAND, H. J. & FARMER, D. M. 1980 Circulation and energetics of a deep, strongly stratified inlet. *Can. J. Fisheries and Aquatic Sci.* **37**, 1398–1410.

GARGETT, A. E. 1980 Data Report and calibrations for turbulence measurements in Knight Inlet, B.C. from the *Pisces IV* submersible: November 1978. *Pacific Mar. Sci. Rep.* 80–6, *Inst. Ocean Sci. Patricia Bay, Sidney, B.C.* 71 pp.

GARGETT, A. E. 1982 Turbulence measurements from a submersible. *Deep-Sea Res.* **29(A)**, 1141–1158.

GARGETT, A. E., HENDRICKS, P. J., SANFORD, T. B., OSBORN, T. R. & WILLIAMS, A. J. 1981 A composite spectrum of vertical shear in the upper ocean. *J. Phys. Oceanogr.* **11**, 1258–1271.

GARGETT, A. E. & OSBORN, T. R. 1981 Small-scale shear measurements during the Fine and Microstructure Experiment (FAME). *J. Geophys. Res.* **86**, 1929–1944.

GARRATT, J. R. 1972 Studies of turbulence in the surface layer over water (Lough Neagh). Part II. Production and dissipation of velocity and temperature fluctuations. *Q. J. R. Met. Soc.* **98**, 642–657.

GIBSON, C. H. 1980 Fossil temperature, salinity and vorticity turbulence in the ocean. In *Marine Turbulence* (ed. J. C. J. Nihoul), pp. 221–258. Elsevier.

GIBSON, C. H. & MASIELLO, P. J. 1972 Observations of the variability of dissipation rates of turbulent velocity and temperature fields. In *Statistical Models and Turbulence* (ed. M. Rosenblatt & C. Van Atta). Lecture Notes in Physics vol. 12, pp. 427–453. Springer.

GIBSON, M. M. 1963 Spectra of turbulence in a round jet. *J. Fluid Mech.* **15**, 161–173.

GRANT, H. L., HUGHES, B. A., VOGEL, W. M. & MOILLIETT, A. 1968 The spectrum of temperature fluctuations in turbulent flow. *J. Fluid Mech.* **34**, 423–442.

GRANT, H. L., STEWART, R. W. & MOILLIET, A. 1962 Turbulence spectra from a tidal channel. *J. Fluid Mech.* **12**, 241–263.

JENKINS, G. M. & WATTS, D. G. 1968 *Spectral Analysis and Its Applications.* Holden-Day.

KAIMAL, J. C., WYNGAARD, J. C. & HAUGEN, D. A. 1968 Deriving power spectra from a 3-D sonic anemometer. *J. Appl. Met.* **7**, 827–837.

KOLMOGOROFF, A. N. 1941 The local structure of turbulence in an incompressible viscous fluid for very large Reynolds number. *C.R. Acad. Sci. USSR* **30**, 301–305.

KOLMOGOROFF, A. N. 1962 A refinement of previous hypotheses concerning the local structure of turbulence in a viscous incompressible fluid at high Reynolds number. *J. Fluid Mech.* **13**, 82–85.

LANGE, R. E. 1982 An experimental study of turbulence behind towed biplanar grids in a salt-stratified fluid. *J. Phys. Oceanogr.* **12**, 1506–1513.

LUECK, R. G. 1980 The calibration of a hot film turbulence probe. *J. Geophys. Res.* **85**, 4923–4932.

LUECK, R. G., CRAWFORD, W. R. & OSBORN, T. R. 1983 Turbulent dissipation over the continental slope off Vancouver Island. *J. Phys. Oceanogr.* **13**, 1809–1818.

MESTAYER, P. 1982 Local isotropy in a high-Reynolds-number turbulent boundary layer. *J. Fluid Mech.* **125**, 475–503.

MILES, J. & HOWARD, L. N. 1964 Note on a heterogeneous shear flow. *J. Fluid Mech.* **20**, 331–336.

MONIN, A. S. & YAGLOM, A. M. 1975 *Statistical Fluid Mechanics*, vol. 2. MIT Press.

NASMYTH, P. W. 1970 Oceanic turbulence. Ph.D. thesis. Institute of Oceanography, University of British Columbia.

NEUMANN, G. & PIERSON, W. J. 1966 *Principles of Physical Oceanography.* Prentice-Hall.

NINNIS, R. 1984 The spatial transfer function of the airfoil shear probe. Ph.D. thesis, Department of Oceanography, University of British Columbia, Vancouver.

OAKEY, N. S. 1982 Determination of the rate of dissipation of turbulent energy from simultaneous temperature and velocity shear microstructure measurements. *J. Phys. Oceanogr.* **12**, 256–271.

OAKEY, N. S. & ELLIOTT, J. A. 1982 Dissipation within the surface mixed layer. *J. Phys. Oceanogr.* **12**, 171–185.

OSBORN, T. R. & CRAWFORD, W. R. 1980 An airfoil probe for measuring turbulent velocity fluctuations in water. In *Air-Sea Interaction: Instruments and Methods* (ed. F. Dobson, L. Hasse & R. Davis), chap. 19. Plenum.

OZMIDOV, R. V. 1965 On the turbulent exchange in a stably stratified ocean. *Izv. Atmos. Oceanic Phys.* **1**, 853–860.

SIDDON, T. E. 1971 A miniature turbulence gauge utilizing aerodynamic lift. *Rev. Sci. Instrum.* **42**, 653–656.

SMITH, J. D. 1974 Turbulent structure of the surface boundary layer in an ice-covered ocean. *Rapp. P.-V. Reun. Cons. Int. Explor. Mer* **167**, 53–65.

STEWART, R. W. 1969 Turbulence and waves in a stratified atmosphere. *Radio Sci.* **4**, 1269–1278.

STILLINGER, D. C., HELLAND, K. N. & VAN ATTA, C. W. 1983 Experiments on the transition of homogeneous turbulence to internal waves in a stratified fluid. *J. Fluid Mech.* **131**, 91–122.

TENNEKES, H. 1973 Intermittency of the small-scale structure of atmospheric turbulence. *Boundary-Layer Met.* **4**, 241–250.

TENNEKES, H. & LUMLEY, J. L. 1972 *A First Course in Turbulence.* MIT Press.

YAGLOM, A. M. 1966 The influence of fluctuations in energy dissipation on the shape of turbulence characteristics in the inertial interval. *Sov. Phys. Dokl.* **11**, 26.